# Multistage $CO_2$ sequestration in the subduction zone: insights from exhumed carbonated serpentinites, SW Tianshan UHP belt, China

Weigang Peng [a,b], Lifei Zhang [a*], Manuel D. Menzel [c],

Alberto Vitale Brovarone [d], Simone Tumiati [b], Tingting Shen [e], Han Hu [a]

[a] *MOE Key Laboratory of Orogenic Belts and Crustal Evolution, School of Earth and Space Sciences, Peking University, Beijing 100871, China*

[b] *Dipartimento di Scienze della Terra, Università degli Studi di Milano, via Mangiagalli 34, 20133, Milano, Italy*

[c] *Instituto Andaluz de Ciencias de la Tierra (IACT), CSIC-UGR, Av. Palmeras 4, 18100 Armilla, Spain*

[d] *Institut de Minéralogie, de Physique des Matériaux et de Cosmochimie UMR 7590 CNRS-UPMC-IRD-MNHN, Campus Jussieu, Case courrier 115, 4 Place Jussieu, 75005 Paris, France*

[e] *Institute of Geology, Chinese Academy of Geological Sciences, Beijing 100037, China*

**[*]Corresponding author**

Lifei Zhang; E-mail:lfzhang@pku.edu.cn

**Abstract**

Climate is regulated by the carbonate–silicate cycle in which slab release and volcanic degassing of $CO_2$ are an important part. However, the mechanisms of C mobility in subduction zones remain largely unresolved. Previous research has focused mainly on investigating the upward transfer of slab-derived carbonic fluids for the forearc mantle metasomatism and partial melting. Furthermore, percolation of $CO_2$-bearing fluids parallel to the downgoing plates can potentially drive carbonation of subducted rocks, which influences the global estimates of C fluxes at convergent margins. Nevertheless, the geological conditions and processes leading to the carbonation of subduction-zone lithologies by fluid–rock interactions are still poorly understood. Here, we present new field, petrological, and isotopic results of carbonated serpentinites — high-pressure (HP) ophidolomites and low-pressure (LP) ophimagnesites and listvenites—from the Chinese southwestern Tianshan HP–UHP metamorphic belt. These rocks recorded the carbonation of subduction-zone serpentinites at HP and LP conditions during exhumation, reflecting the multistage transfer and infiltration of carbonic fluids along the plate boundary. The HP ophidolomites are characterized by the growth of carbonates (dolomite, aragonite, and Mg-calcite) at the expense of silicates in the host serpentinites. Integrated Sr–C–O isotopic data and thermodynamic modelling suggest that carbonic fluids (containing a

$CO_{2,aq}$ concentration of up to 1.9 molal) emanating from carbonate-bearing metamafic rocks (e.g., eclogites) likely contributed to HP carbonation of serpentinites at ca. 15–25 kbar and 550–600 °C. The close contact of ophidolomites and carbonated metasedimentary rocks in the field as well as their similarities in Sr isotope compositions suggest that the latter could also have acted as the possible C source. Alternatively, both lithologies may have formed by coupled HP carbonation along the lithological interface between serpentinites and metasedimentary rocks. Subsequent fluid–rock interactions at relatively shallow crustal levels resulted in a second stage of serpentinite carbonation to form LP ophimagnesites and listvenites, during which the metasomatic $CO_2$-bearing fluids may have originated from metasedimentary rocks. The multistage $CO_2$ sequestration in subduction-zone serpentinites implies that hydrated ultramafic rocks in subducted slabs are highly effective reactants to capture and store slab-released C over a wide range of *P–T* conditions, with the potential to substantially control the C distribution between shallow and deep reservoirs and thus modulate C fluxes in subduction zones.

*Keywords:* Subduction; Carbonation; Serpentinite; Fluid–rock interactions; Exhumation; Chinese southwestern Tianshan

## 1. Introduction

Convergent margins play a significant role in the global C cycle by recycling crustal C (mainly carbonates) into the mantle via subduction and back to the surface via partial melting and volcanism (e.g., Berner, 1999; Dasgupta and Hirschmann, 2010; Manning, 2014). Oceanic sediments and altered mafic and ultramafic rocks of the oceanic lithosphere are dominant carbonate-bearing lithologies in subducted slabs (e.g., Plank and Langmuir, 1998; Jarrard, 2003; Dasgupta and Hirschmann, 2010; Alt et al., 2013; Kelemen and Manning, 2015). However, the mechanisms through which C in these lithologies is mobilized in subduction zones remain controversial. For decades, both thermodynamic modelling (Kerrick and Connolly, 1998, 2001a, 2001b; Gorman et al., 2006) and experimental investigation (Molina and Poli, 2000; Thomsen and Schmidt, 2008; Tsuno and Dasgupta, 2011) have elucidated that substantial quantities of C can be retained in subducted slabs beyond subarc depths without experiencing prominent decarbonation reactions. Conversely, recent research has indicated that fluid-induced dissolution of carbonates in subducted slabs may represent an essential pathway for the release of carbonic fluids (Frezzotti et al., 2011; Ague and Nicolescu, 2014). Hence, a reevaluation of C fluxes in subduction zones has proposed that most subducted C could be transferred into the overlying plate at forearc to subarc depths, while

relatively little C might be carried into the convecting mantle (Kelemen and Manning, 2015). Nonetheless, eclogite-facies metasomatic rocks formed by interactions with $CO_2$-bearing fluids in Alpine Corsica (France) and the Voltri Massif (Ligurian Alps, Italy) have provided compelling evidence for carbonate precipitation within subducted slabs (Piccoli et al., 2016, 2018; Scambelluri et al., 2016). The retention of C within subducted lithologies forming relatively stable carbonates may potentially supply C for arc magmatism and/or recycle C into the convecting mantle (Sieber et al., 2018).

Serpentinites are highly effective reactants for carbonation reactions when in contact with $CO_2$-bearing fluids (e.g., Power et al., 2013), forming partly and completely carbonated rocks such as ophicarbonates (e.g., Scambelluri et al., 2016) and listvenites (e.g., Hansen et al., 2005; Falk and Kelemen, 2015; Menzel et al., 2018). The carbonation of serpentinites has been the subject of increasing attention due to its role in the global $CO_2$ sequestration (Power et al., 2013) and the deep Earth C cycle (Sieber et al., 2018). Extensive studies have focused mainly on investigating the carbonation of serpentinized mantle wedge driven by upward migration of slab-derived carbonic fluids, which can accumulate significant amounts of C in forearc settings to account for the imbalance between C release from subducted slabs and C emission from arc volcanoes (Falk and Kelemen, 2015; Kelemen and Manning, 2015;

Menzel et al., 2018; Sieber et al., 2018). By contrast, the understanding of fluid–rock interactions that lead to the carbonation of subducted serpentinites is largely incomplete (Scambelluri et al., 2016; Piccoli et al., 2018). This calls for additional efforts to characterize the carbonation processes in serpentinites from subduction zones.

In this study, we report the occurrence of carbonated serpentinites (HP ophidolomites and LP ophimagnesites and listvenites) formed by fluid–rock interactions from the Chinese southwestern Tianshan HP–UHP metamorphic belt. We show and discuss petrology, geochemistry, and thermodynamic modelling of the two carbonation processes during different stages of exhumation from HP conditions to relatively shallow crustal levels. Finally, we discuss the general implications of serpentinite carbonation within subduction zones on the deep C cycle and evaluate the C sequestration potential of subduction-zone serpentinites at both HP and LP conditions.

## 2. Geological setting

The Chinese southwestern Tianshan metamorphic belt is the largest oceanic-type HP–UHP metamorphic belt worldwide (Zhang et al., 2018), which formed due to northward subduction of the Tarim Plate underneath the Yili-Central Tianshan Plate (Fig. 1a; Zhang et al., 2013). This HP–UHP metamorphic belt consists of various lithologies, including garnet–

phengite schists, marbles, blueschists, eclogites, and serpentinites with associated rodingites (Shen et al., 2015). Serpentinite blocks are mostly exposed at Changawuzi in an area of about 6–10 $km^2$ (Fig. 1b and c) and their protoliths include harzburgites, wehrlites, and dunites (Shen et al., 2015). Detailed investigation has revealed two stages of serpentinization: (1) a seawater-related alteration of oceanic mantle rocks subsequently overprinted by the UHP metamorphism ($P$ = 37 ± 7 kbar, $T$ = 510–530 °C) during subduction (Shen et al., 2015) and (2) a later rehydration of metamorphic or primary olivine and pyroxene in the serpentinites at relatively shallow crustal levels during exhumation (i.e., retrograde serpentinization; Li et al., 2007, 2010).

The HP metamorphic veins occur extensively in blueschists and eclogites from the Chinese southwestern Tianshan, indicating the pervasive fluid production and percolation during metamorphism (e.g., Gao and Klemd, 2001; Gao et al., 2007; John et al., 2008; van der Straaten et al., 2008, 2012; Beinlich et al., 2010; Lü et al., 2012; Zhang et al., 2016). Most of these HP veins are thought to represent the fluid-induced mass transport during progressive dehydration of blueschists into eclogites (e.g., Gao and Klemd, 2001; Gao et al., 2007; John et al., 2008; Beinlich et al., 2010). In contrast, retrograde HP veins have also been increasingly recognized (e.g., Lü et al., 2012; Zhang et al., 2016), indicating the fluid-mediated element mobility at HP conditions during

exhumation evidenced by the identification of retrograde blueschist-facies overprint on eclogites (van der Straaten et al., 2008, 2012). Our study targets some additional aspects of metamorphic fluid percolation in the Chinese southwestern Tianshan, particularly regarding the response of subduction-zone serpentinites to the reactive $CO_2$-bearing fluids during exhumation from HP conditions to relatively shallow crustal levels that has remained poorly investigated to date.

## 3. Sample occurrence and description

The herein studied carbonated serpentinites (ophidolomites, ophimagnesites, and listvenites) are intimately associated with UHP serpentinites in the field. Besides, (retrograde) eclogites and blueschists also occur in the serpentinite blocks. All of these lithologies are distributed in the vicinity of carbonate-bearing mica schists and carbonated mica schists (Fig. 2a), which are distinguished by their considerably different carbonate contents and Sr–C–O isotopic compositions (see Section 6.1.1 and Peng et al., 2018).

### *3.1. Ophidolomites*

Field observations indicate that ophidolomites, in association with (retrograde) eclogites and blueschists, are exposed at the top of UHP serpentinites and show close contact with carbonated mica schists (Fig. 2b and c). Ophidolomites, which in some cases require microscopic

observations to be distinguished from carbonate-free serpentinites, are commonly characterized by dolomite grains scattering in and/or dolomite veins cutting across the host serpentinites (Fig. 3a and b). These samples are mainly composed of dolomite, antigorite, chlorite, and diopside or tremolite, with or without aragonite, Mg-calcite, calcite, olivine, and brucite (Table 1). The carbonate content was petrographically estimated from < 1 vol% to ~10 vol%. Ophidolomites occur with variable microstructures in different samples. In homogeneous ophidolomites, euhedral to subhedral dolomite grains (ranging in size from hundreds of micrometers to several millimeters) are evenly distributed in the matrix of antigorite and chlorite (Fig. 4a and b). Ilmenite enclosed in dolomite often has inclusions of antigorite, chlorite, and diopside (Fig. 4c). In contrast, carbonation in inhomogeneous ophidolomites occurs mainly within local domains, where carbonates (dolomite, aragonite, and Mg-calcite) grow at the expense of diopside (having antigorite inclusions; Fig. 4d–f). Occasionally, in several ophidolomites, dolomite veins and grains replace antigorite and tremolite (having antigorite inclusions) in the matrix of antigorite (Fig. 4g–i).

### *3.2. Ophimagnesites and listvenites*

Ophimagnesites and listvenites occur in close contact with carbonate-bearing mica schists in the field (Fig. 2d). Ophimagnesites are mainly characterized by magnesite grains and veins filled in the host

serpentinites (Fig. 3c). They mainly consist of magnesite and antigorite, with or without dolomite, chrysotile, and talc (Table 1). The carbonate content was petrographically evaluated from ~10 vol% to ~15 vol%. Carbonate occurrences of ophimagnesites include (1) late magnesite-bearing chrysotile veins cross-cutting the host serpentinites (Fig. 5a and b), and (2) magnesite grains (ranging in size from less than one millimeter to several millimeters) distributed in the matrix of antigorite, with or without talc (Fig. 5c and d).

Listvenites commonly enclose serpentinite and ophimagnesite relicts in the field (Fig. 2d) and are typically characterized by a yellowish weathered surface in the hand specimen (Fig. 3d). However, the presence of fuchsite (Cr-rich mica), a characteristic phase in this rock type, confers a greenish color to the rock (Fig. 3d). These samples are almost completely composed of carbonates (magnesite and dolomite, up to ~50 vol%), quartz, and fuchsite (Fig. 5e and f; Table 1). Fuchsite is related to the decomposition of chromite—a common observation in listvenites (e.g., Halls and Zhao, 1995)—while the rim of fuchsite has occasionally been altered to chlorite (Fig. 5f).

## 4. Methods

### *4.1. Scanning electron microscopy*

Back-scattered electron (BSE) images were recorded with an FEI

Quanta 650 FEG scanning electron microscope (SEM) equipped with an Oxford INCA X-MAX50 250+ energy dispersive X-ray spectrometer at the School of Earth and Space Sciences (SESS), Peking University. The running conditions were 10 kV acceleration voltage, 5 nA beam current, and ~10 mm working distance. Compositional X-ray maps were recorded under the same running conditions (10 kV, 5 nA, ~10 mm), with an integration time of ~360 min.

### *4.2. Raman spectroscopic analyses*

Raman spectroscopy was performed on a Renishaw-inVia Reflex Laser Raman probe using the 532 nm line of a DPSS Laser at SESS, Peking University. The laser power was 50 mW and the laser spot was 1 μm, with an accumulation time varying between 5 s and 10 s. The estimated spectral resolution was higher than 1.0 $cm^{-1}$ and calibration was performed using synthetic silicon. Serpentine group minerals (e.g., antigorite, lizardite, and chrysotile) and calcium carbonate phases (e.g., aragonite and calcite) were identified with the peak assignments from Rinaudo et al. (2003) and Edwards et al. (2005), respectively.

### *4.3. Mineral chemistry*

Major elements of minerals were analyzed with a JEOL 8230 electron microprobe analyzer at SESS, Peking University, using 15 kV acceleration voltage and 10 nA beam current. The SPI 53 minerals standard (U.S.) was adopted for the quantitative analysis (following Li et

al., 2018): sanidine (K), diopside (Ca and Mg), rutile (Ti), jadeite (Na, Al, and Si), chromium oxide (Cr), rhodonite (Mn), hematite (Fe), and nickel silicide (Ni). The beam diameter was 2 μm for all minerals except for fuchsite (5 μm) and calcium carbonates (5–10 μm). The PRZ correction was performed at the final calibration stage.

### *4.4. Bulk-rock major and trace element analyses*

After removing weathered surfaces, rock chips were cut from the homogeneous parts of the samples. Then, they were cleaned in distilled water, crushed in a corundum jaw crusher to 60 mesh, and further ground in an agate mill to < 200 mesh. About 30 mg of powder of each sample was used for the bulk-rock major element analysis, performed with a Leeman Prodigy inductively coupled plasma optical emission spectroscopy (ICP-OES) system with high-dispersion Echelle optics at China University of Geosciences, Beijing. Precisions (1σ) for $SiO_2$ (0.50%), $TiO_2$ (2.20%), $Al_2O_3$ (1.20%), $TFe_2O_3$ (2.30%), MnO (3.00%), MgO (1.70%), CaO (2.70%), $Na_2O$ (1.90%), $K_2O$ (1.80%), and $P_2O_5$ (2.50%) were calculated based on rock standards GSR-3 [National Geological Standard Reference Materials (SRM) of China] and AGV-2 [United States Geological Survey (USGS)]. Loss on ignition (LOI) was determined by placing 1 g of sample powder in a furnace at 1000 °C for several hours before being cooled in a desiccator and reweighed (Song et al., 2010).

Bulk-rock trace elements were analyzed with an Agilent 7500Ce inductively coupled plasma mass spectrometer (ICP-MS) at SESS, Peking University. For detailed explanation and description, see Song et al. (2010). Four national geological standard reference materials of China (GSR-1, GSR-3, GSR-12, and DZS-1) were used to monitor the analytical accuracy and precision. In this study, only Rb and Sr contents, with their relative differences better than 10%, are reported for the recalculation of Sr isotope compositions (see below).

### *4.5. Sr isotopic analyses*

We selected two pure serpentinites, six ophidolomites, seven ophimagnesites, and nine listvenites for the whole-rock Sr isotopic analysis. For comparison, carbonates separated from representative ophidolomites and listvenites were also measured (see Zhu et al., 2018 for detailed separation procedures). Separation and purification processes of Rb and Sr were carried out using conventional ion exchange procedures in the ultraclean laboratory at SESS, Peking University. The Sr isotopic ratios were measured using a Thermo-Finnigan Triton thermal ionization mass spectrometer (TIMS) at the State Key Laboratory of Isotope Geochemistry, Guangzhou Institute of Geochemistry, Chinese Academy of Sciences. The ratios of $^{87}Rb/^{86}Sr$ were calculated based on the Rb and Sr contents determined by ICP-MS (described above). The mass fractionation was corrected by normalizing the measured $^{87}Sr/^{86}Sr$

against $^{86}Sr/^{88}Sr$ ratio of 0.1194. Rock standard BCR-2 was used to evaluate the separation and purification processes of Rb and Sr, yielding a weighted mean $^{87}Sr/^{86}Sr$ ratio of 0.705009 ± 0.000008 (2σ, n = 10). The National Bureau of Standards 987 Sr standard was also analyzed and gave a weighted mean $^{87}Sr/^{86}Sr$ ratio of 0.710245 ± 0.000005 (2σ, n = 10).

### *4.6. C and O isotopic analyses*

C and O isotope compositions of carbonates were determined by the production of $CO_2$ after reaction with 0.2 ml phosphoric acid at 72 ± 0.1 °C for 24 h. These samples were analyzed on a Thermo Fisher MAT-253 using GasBench II at the Laboratory for Stable Isotope Geochemistry, Institute of Geology and Geophysics, Chinese Academy of Sciences. Standard deviations of $\delta^{13}C$ and $\delta^{18}O$ values were better than 0.15‰ and 0.20‰, respectively, calculated from replicate analyses of an internal laboratory calcite standard. The measured values of $\delta^{13}C$ and $\delta^{18}O$ are reported relative to the Vienna Pee Dee Belemnite (V-PDB) and Vienna Standard Mean Ocean Water (V-SMOW), respectively.

### *4.7. Thermodynamic modelling*

#### *4.7.1. Pseudosection modelling*

Pseudosections were calculated with the software package Perple_X (http://www.perplex.ethz.ch; Connolly, 2005), using the thermodynamic database of Holland and Powell (1998) revised in 2002 (hp02ver.dat). All

applied solid solution models and their sources are provided in Supplementary Table S1. The compensated Redlich–Kwong (CORK) equation of state (EoS) from Holland and Powell (1991) was used for $H_2O$–$CO_2$ fluids (F).

*4.7.2. Modelling of fluid composition and speciation*

The composition and speciation of fluids in equilibrium with ophidolomite and carbonate-bearing eclogite along the retrograde metamorphic *P–T* path of the Tianshan (Zhang et al., 2018) were calculated using the Deep Earth Water (DEW) aqueous database (revised version after Huang and Sverjensky, 2019) implemented with Perple_X (Connolly and Galvez, 2018). The attained fluid compositions correspond to those of the pervasively infiltrated fluids in overall equilibrium with ophidolomite in the Ca–Fe–Mg–Al–Si–C–O–H system (Sample C1518; Table 5) and carbonate-bearing eclogite in the Na–Ca–K–Fe–Mg–Al–Si–C–O–H system (Sample L0910 from Li et al., 2014). The redox budget of the rock compositions was fixed by assuming all C to be $CO_2$ and $Fe^{3+}/Fe^{tot} = 0.15$ for ophidolomite (consistent with the lack of graphite and hematite in the rock) and $Fe^{3+}/Fe^{tot} = 0.19$ for carbonate-bearing eclogite (Li et al., 2014). The calculations were performed based on a COH-Fluid as solvent phase to attain the initial phase equilibrium and chemical potentials of the system components, from which activity relations of solute aqueous species were derived using pH to balance charge (Galvez

et al., 2015). The initial solution, back-calculated from the chemical potentials, was subsequently refined by the code to attain overall equilibrium and mass-balance between solids, solvent, and solutes (Connolly and Galvez, 2018). We applied the same solid solution models as in the previous pseudosection modelling (Supplementary Table S1) and the CORK EoS for the solvent $H_2O$ and $CO_2$. Besides, the modified Redlich–Kwong EoS was used for methane. For consistency with the use of a COH solvent, the neutral C species $CO_{2,aq}$, $H_2CO_{3,aq}$, and methane were excluded from the DEW database for the calculations. The revised DEW database (Huang and Sverjensky, 2019) further includes the species $MgOSi(OH)_2(HCO_3)^+$ to fit experimental data at 4–5 GPa (Dvir et al., 2011). Given its extrapolation to the lower pressures considered here is somewhat uncertain, we excluded it from the present model, and therefore the total concentrations of Mg, Si, and C were possibly underestimated.

## 5. Results

### *5.1. Mineral compositions*

Representative mineral compositions of the studied carbonated serpentinites are presented in Table 2.

#### *5.1.1. Antigorite*

The compositional analyses of antigorite were normalized to 116

oxygens [$Mg_{x(48-4y)}Fe_{(1-x)(48-4y)}Al_{8y}Si_{34-4y}O_{85}(OH)_{62}$, revised from Padrón-Navarta et al. (2013) after personal communication] assuming $Fe^{tot} = Fe^{2+}$. The negative trend between Al and Si (Fig. 6a) accords with the Tschermak substitution ($Al_2Mg_{-1}Si_{-1}$) in antigorite (Padrón-Navarta et al., 2013). Antigorite in chlorite-free ophimagnesites has a very low Al content of 0.3–0.8 a.p.f.u. (atoms per formula unit). In contrast, ophidolomites commonly contain abundant chlorite and the Al content of antigorite is comparatively higher (0.9–3.5 a.p.f.u.), similar to that of UHP low-Al and retrograde high-Al antigorite in the associated serpentinites (Fig. 6a). In addition, antigorite in ophidolomites and ophimagnesites have $X_{Mg}$ [Mg/(Mg + Fe)] values of 0.88–0.97 and 0.89–0.93, respectively.

*5.1.2. Carbonates*

Dolomite in ophidolomites shows no zoning and has $X_{MgCO3}$ [Mg/(Ca + Mg + Fe)] and $X_{Mg}$ values of 0.44–0.49 and 0.92–1.00, respectively. Mg-calcite in the ophidolomite C1531-2 displays $X_{MgCO3}$ values of 0.11–0.13 (three measurements), substantially higher than those of the nearly pure Ca-carbonate (i.e., aragonite) in this rock (Fig. 6b). Magnesite in ophimagnesites and listvenites is commonly zoned and has variable $X_{MgCO3}$ values of 0.86–0.97 and 0.81–0.97, respectively. This zonation of magnesite, with the cores showing higher $X_{MgCO3}$ while the rims showing lower $X_{MgCO3}$, is typical for listvenites ( e.g., Hansen et al., 2005; Menzel

et al., 2018).

*5.1.3. Other minerals*

The $X_{Mg}$ values are 0.91–0.98 for diopside [$Ca_{(0.99–1.01)}Mg_{(0.89–0.98)}Fe_{(0.02–0.09)}Si_{(1.96–2.01)}O_6$], 0.93–0.95 for tremolite [$Ca_{(1.76–1.91)}Mg_{(4.53–4.67)}Fe_{(0.26–0.32)}Si_{(8.00–8.13)}O_{22}(OH)_2$], and 0.89–0.96 for chlorite [$Mg_{(4.37–5.07)}Fe_{(0.23–0.58)}Si_{(3.02–3.45)}Al_{(1.23–2.03)}O_{10}(OH)_8$] in ophidolomites. In general, $X_{Mg}$ values of these silicates (including antigorite) overlap with those of dolomite, in agreement with the petrographically recognized dolomite growth at the expense of silicates in ophidolomites (Fig. 4). Antigorite and talc in ophimagnesites have $X_{Mg}$ values of 0.89–0.93 and 0.93–0.96, respectively, reflected by the larger variation in $X_{MgCO3}$ of magnesite (see above). Fuchsite in listvenites shows high $Cr_2O_3$ contents (8.56–11.89 wt%), pointing to its formation by consumption of chromite (Fig. 5f).

***5.2. Sr isotope compositions***

Sr isotope compositions of the studied serpentinites, carbonated serpentinites, and representative carbonate separates are listed in Table 3.

The initial $^{87}Sr/^{86}Sr$ ratios of ophidolomites and the carbonate separates were recalculated for an age of 320 Ma, the time of HP–UHP metamorphism in the Chinese southwestern Tianshan orogenic belt (Zhang et al., 2018 and references therein). Because of the very low $^{87}Rb/^{86}Sr$ ratios of these samples ($^{87}Rb/^{86}Sr < 0.033$), there are no significant differences between the recalculated initial $^{87}Sr/^{86}Sr$ ratios and the

measured Sr isotope compositions (Table 3). Serpentinites have initial $^{87}Sr/^{86}Sr$ ratios ($t$ = 320 Ma) of 0.7079–0.7088, comparatively higher than those of ophidolomites and the carbonate separates (initial $^{87}Sr/^{86}Sr$ = 0.7064–0.7075; Fig. 7a). In contrast, the age-corrected Sr isotope values of ophidolomites and the carbonate separates are similar with those of the carbonate-bearing eclogites from adjacent localities in the Tianshan (initial $^{87}Sr/^{86}Sr$ = 0.7061–0.7072; van der Straaten et al., 2012) and carbonated mica schists from the study area (initial $^{87}Sr/^{86}Sr$ = 0.7064–0.7068, Fig. 7a; Peng et al., 2018), but considerably lower than those of carbonate-bearing mica schists from the study area (initial $^{87}Sr/^{86}Sr$ = 0.7099–0.7118; Peng et al., 2018).

The initial $^{87}Sr/^{86}Sr$ ratios of ophimagnesites, listvenites, and the carbonate separates were recalculated for an age of 290 Ma, the time when the retrograde serpentinization induced by fluid mobility took place at relatively shallow crustal levels (Li et al., 2010). Compared with the initial $^{87}Sr/^{86}Sr$ ratios ($t$ = 290 Ma) of 0.7079–0.7088 for serpentinites, however, ophimagnesites, listvenites, and the carbonate separates mostly show comparatively higher Sr isotope compositions (Fig. 7b). In detail, the initial $^{87}Sr/^{86}Sr$ ratios of ophimagnesites (0.7089–0.7104) generally overlap with those of listvenites and the carbonate separates (initial $^{87}Sr/^{86}Sr$ = 0.7083–0.7109), whereas one listvenite sample displays a lower initial $^{87}Sr/^{86}Sr$ ratio of 0.7068 (Fig. 7b).

### *5.3. C and O isotope compositions of carbonates*

C and O isotope compositions of carbonates in the studied carbonated serpentinites are presented in Table 4.

Carbonates in ophidolomites have $\delta^{13}C$ values ranging from –3.6‰ to –0.3‰ and $\delta^{18}O$ values from +10.5‰ to +13.3‰. Carbonates in ophimagnesites and listvenites have similar C and O isotope compositions, showing relatively uniform $\delta^{13}C$ (mostly –4.1‰ to –1.8‰) but more variable $\delta^{18}O$ (mostly +12.7‰ to +18.3‰; Fig. 8). However, one ophimagnesite sample displays lower C and O isotope values ($\delta^{13}C$ = –5.7‰ and $\delta^{18}O$ = +12.5‰). In general, $\delta^{13}C$ values of carbonates in the carbonated serpentinites are slightly lower than those of marine carbonates (Hoefs, 2009), but overlap with C isotope compositions of carbonate-bearing lithologies (e.g., eclogites and mica schists) from Tianshan (Fig. 8; Collins et al., 2015; Peng et al., 2018; Zhu et al., 2018).

### *5.4. Results of pseudosections*

#### *5.4.1. PT constraints of the homogeneous ophidolomite (C1518)*

Based on the mineral assemblages and compositions, the system CFMASH–$CO_2$ (CaO–FeO–MgO–$Al_2O_3$–$SiO_2$–$H_2O$–$CO_2$) was chosen to compute *P–T* pseudosections for the homogeneous ophidolomite (C1518), in which dolomite is evenly distributed (Figs. 3a and 4a & b). Although $H_2O$ and $CO_2$ are commonly presumed to be saturated fluid phases when performing thermodynamic modelling of carbonate-bearing

metamorphic rocks (e.g., Sieber et al., 2018), the specification of $H_2O$ and $CO_2$ as the thermodynamic components may yield more realistic results (e.g., Kerrick and Connolly, 1998, 2001a, 2001b; Li et al., 2012, 2013, 2014; Scambelluri et al., 2016; Menzel et al., 2019). Hence, the effective bulk-rock composition was derived from mineral compositions and modes (Table 5), in which the $H_2O$ and $CO_2$ contents were calculated based on the abundances of hydrous minerals and carbonates in the sample (e.g., see Li et al., 2012 for similar approaches). The estimated $CO_2$ content (2.53 wt%; Table 5) is plausible since it is similar to that of HP ophidolomites ($CO_2$ = 3 wt%) from comparable metamorphic settings (Scambelluri et al., 2016). Moreover, the calculated nonvolatile components (i.e., CaO, FeO, MgO, $Al_2O_3$, and $SiO_2$) in the effective bulk-rock composition approximate those measured by the ICP-OES analysis (Table 5), both of which were further used for $T$–$X_{CO2}$ pseudosections in the CFMASH–$CO_2$ system (with saturated $H_2O$ and $CO_2$) at 2 GPa (Supplementary Fig. S1) to evaluate the dependence of phase stabilities on slight variations in the bulk-rock composition. As a result, the very similar topologies of $T$–$X_{CO2}$ pseudosections (Supplementary Fig. S1) suggest that a slight variation in the bulk-rock composition (within the uncertainty) does not significantly affect the phase stabilities.

In the $P$–$T$ phase diagram, the mineral assemblage Chl + F + Ol + Atg

+ Di + Dol and the Al content of antigorite [$y_{Atg}$ = 0.335 ± 0.022 (n = 24), where $y_{Atg}$ = Al/8 in a.p.f.u.; Padrón-Navarta et al., 2013] yielded a well-constrained temperature of ca. 555–595 °C but a less precise pressure of ca. 14–24 kbar (Fig. 9a) for the ophidolomite. The mineral proportions predicted by the thermodynamic modelling at these *P–T* conditions are in overall agreement with the observed phase proportions, whereas the absence of olivine in the rock is likely ascribed to the retrograde serpentinization at relatively shallow crustal levels (Li et al., 2007, 2010). In order to test the effect of olivine, we recalculated the *P–T* pseudosection using the olivine-existing bulk-rock composition (Supplementary Table S2) that was simply integrated by involving olivine modes (ca. 2 vol%; Fig. 9a) and compositions from the associated UHP serpentinites (Shen et al., 2015). The recalculated *P–T* conditions (ca. 15–25 kbar and 560–600 °C; Supplementary Fig. S2a) show no significant differences, which in turn suggests that the phase stabilities are largely unaffected by the slight variation in the bulk-rock composition. In addition, the calculated $X_{CO2}$ [$CO_2$/($H_2O$ + $CO_2$)] in the metasomatic $CO_2$-bearing fluids is ranging from 0.0005 to 0.005 (Fig. 9a and Supplementary Fig. S1 & S2a) for the stability of the HP ophidolomite.

*5.4.2. PT constraints of the inhomogeneous ophidolomite (C1531-2)*

Given the metasomatic inhomogeneity of the whole rock (C1531-2), where carbonation mainly occurs within the local domain (Fig. 4d), we

derived the local composition (Table 5) by integrating mineral compositions and modes of phases in the domain to compute *P–T* pseudosections in the CFMASH–$CO_2$ system. In general, the calculated local composition is comparable to the measured bulk-rock composition, but there are small compositional differences (e.g., CaO) likely due to the enrichment of minerals (e.g., diopside) in this domain relative to the whole rock (Table 5).

The presence of aragonite and Mg-calcite in the ophidolomite (Fig. 4d–f) provides evidence for the relatively high *P–T* conditions, similar to the observations from subducted meta-ophicarbonates elsewhere (e.g., Menzel et al., 2019). The Mg-calcite is one of the four phases (aragonite, Mg-calcite, dolomite, and magnesite) constituting the Ca–Mg carbonate system at HP subsolidus conditions (Goldsmith and Newton, 1969), and formed due to the retrograde decomposition of dolomite and aragonite (Dol + Arg → Mg-Cal; e.g., Hermann et al., 2016). In particular, the composition of Mg-calcite can be used to estimate the minimum temperature of the reequilibration during retrograde metamorphism (e.g., Anovitz and Essene, 1987; Mposkos et al., 2006; Hermann et al., 2016; Menzel et al., 2019). The phase relations in the $CaCO_3$–$MgCO_3$–$FeCO_3$ system (Anovitz and Essene, 1987) and the experimentally determined Fe-free calcite–dolomite solvus (Supplementary Fig. S3; Hermann et al., 2016) suggest that the $X_{MgCO3}$ values of Mg-calcite (0.11–0.13; Table 2)

in this rock correspond to temperatures of ca. 650–700 °C. Nevertheless, the temperature estimates for the retrograde reequilibration are higher than the thermodynamically calculated temperatures for the formation of the ophidolomite ($T$ = ca. 570–620 °C; see below) and the metamorphic peak temperatures of the Tianshan (Supplementary Fig. S3; Tan et al., 2017 and references therein). This overestimation is probably owing to (1) disequilibrium of these carbonate assemblages during retrogression (Anovitz and Essene, 1987), (2) contamination of Mg to the micrometer-sized Mg-calcite (Fig. 4d and e) from the associated Mg-rich silicates (e.g., antigorite and chlorite) during analysis as reflected by the $SiO_2$ contents of 0.09–0.18 wt% in Mg-calcite (Table 2), and (3) errors of the temperature estimates from the phase relations in the $CaCO_3$–$MgCO_3$–$FeCO_3$ system (Anovitz and Essene, 1987) and no consideration of Fe in the experimentally determined calcite–dolomite solvus (Hermann et al., 2016). Overall, $P$–$T$ conditions of the inhomogeneous ophidolomite ($P$ > 14–15 kbar, $T$ = ca. 570–620 °C; Fig. 9b) constrained by the mineral assemblage (Chl + F + Ol + Atg + Di + Dol) and the experimentally determined aragonite–Mg-calcite transition (Hermann et al., 2016) are similar with those of the homogeneous ophidolomite (see Section 5.4.1). Also, the absence of olivine in the inhomogeneous ophidolomite is likely due to the retrograde serpentinization (Li et al., 2007, 2010). However, the recalculated $P$–$T$ conditions using the simply integrated olivine-

existing local composition (Supplementary Table S2) gave similar results (Supplementary Fig. S2b), even though the involvement of olivine (ca. 6 vol% by calculation; Fig. 9b) decreased the $H_2O$ content. In addition, $X_{CO2}$ in the metasomatic $CO_2$-bearing fluids responsible for the inhomogeneous HP ophidolomite is lower than 0.005 (Fig. 9b and Supplementary Fig. S2b), comparable to that in equilibrium with the homogenous HP ophidolomite (see Section 5.4.1).

## 6. Discussion

### *6.1. Ophidolomites: mobility and precipitation of $CO_2$-bearing fluids at high pressures*

Marine-originated ophicarbonates (commonly called ophicalcites) typically show features of serpentinite clasts cemented by carbonate matrix (e.g., Bonatti et al., 1974; Lafay et al., 2017) or fractured serpentinites filled by carbonate veins (e.g., Früh-Green et al., 2003, 2018; Kelley et al., 2005; Bach et al., 2011). In contrast, the studied ophidolomites are characterized by dolomite grains and/or veins replacing silicate minerals (e.g., antigorite, diopside, and tremolite; Figs. 3a, b and 4), pointing to interactions between $CO_2$-bearing fluids and serpentinites during metamorphism. The similar $X_{Mg}$ values of dolomite and silicates (see Section 5.1) likely represent the compositional inheritance during fluid–rock interactions. In particular, ilmenite enclosed

in dolomite grains often has inclusions of antigorite, chlorite, and diopside (Fig. 4c), suggesting the metamorphic genesis of ilmenite and dolomite. Hence, the integrated microstructures and mineral compositions demonstrate that the carbonation of serpentinites took place in the subduction zone rather than in the marine environment. This is reflected by Sr isotope compositions of the studied ophidolomites and carbonate separates distinct from those of the Apenninic ophicarbonates formed by interactions with Cretaceous–Cenozoic seawater (Barbieri et al., 1979) and carbonate cements in ophicarbonates from the Mid-Atlantic Ridge (Fig. 7a; Bonatti et al., 1974). Besides, carbonates in the ophidolomites show lighter $\delta^{18}O$ values than those in seawater-related ophicarbonates from the Alps and Apennine (e.g., Barbieri et al., 1979; Schwarzenbach et al., 2013) and from the Mid-Atlantic Ridge (Fig. 8; Bonatti et al., 1974), which will be discussed in Section 6.1.2.

*6.1.1. Possible C source(s) responsible for the formation of ophidolomites*

The hydration of exposed lithospheric mantle on or close to the ocean floor at a slow-spreading ridge (e.g., Cannat et al., 1997; Bach and Früh-Green, 2010) represents the origin of the Changawuzi UHP serpentinites prior to subduction, as evidenced from the associated rodingites (Li et al., 2007, 2010; Shen et al., 2015, 2016) and seawater-like O isotope compositions of antigorite and serpentinites (Scicchitano et al., 2018). Moreover, the rare preservation of primary olivine and pyroxene in the

serpentinites indicates a high degree of seawater alteration (Shen et al., 2015, 2016). Thus, these serpentinites may have inherited $^{87}Sr/^{86}Sr$ ratios from seawater, because Sr isotope compositions of marine-originated rocks are largely controlled by the initial $^{87}Sr/^{86}Sr$ ratios of seawater and the degree of fluid–rock interactions (e.g., Boschi et al., 2008; Delacour et al., 2008). This is confirmed by Sr isotope compositions of the serpentinites similar with those of Ordovician–Carboniferous (lifetime of the south Tianshan paleocean; Xia et al., 2014) seawater ($^{87}Sr/^{86}Sr$ = ca. 0.7076–0.7092, Fig. 7a; Veizer et al., 1999). Compared with the serpentinites, however, ophidolomites and the carbonate separates display lower initial $^{87}Sr/^{86}Sr$ ratios (Fig. 7a) indicative of Sr isotope exchange with carbonic fluids during metamorphism. Since carbonate-bearing lithologies in the subduction zone can act as the potential C sources (e.g., van der Straaten et al., 2008, 2012; Li et al., 2017), the reactive $CO_2$-bearing fluids responsible for the formation of ophidolomites may have originated from carbonate-bearing eclogites and/or carbonated mica schists as suggested by the close contact of these lithologies in the field (Fig. 2b and c) and their similar initial $^{87}Sr/^{86}Sr$ ratios (Fig. 7a).

The carbonate-bearing eclogites have a widespread distribution at Changawuzi and adjacent localities (e.g., Kebuerte and Habutengsu) in the Tianshan (Fig. 1), containing dolomite/ankerite (ca. 5–20 vol%) as the major carbonate phases (e.g., van der Straaten et al., 2008, 2012; Li et al.,

2012, 2013, 2014; Collins et al., 2015; Tao et al., 2018; Zhu et al., 2018). In several cases, the carbonate-bearing eclogites are characterized by the retrograde blueschist-facies overprint, during which the exchange of elements and volatiles between rocks and slab-derived fluids provides a potential for C release from these carbonate-bearing metamafic rocks (van der Straaten et al., 2008, 2012). Identification of the possible C source from the carbonate-bearing eclogites is complicated by the wide range of C isotope compositions related to carbonate–organic matter reequilibrations and/or decarbonation reactions (Fig.8; Collins et al., 2015; Zhu et al., 2018). In general, the slightly variable but comparatively heavier $\delta^{13}C$ of carbonates in the ophidolomites can reflect the isotopic inheritance from the carbonate-bearing eclogites but without significant contribution of organic C or decarbonation (Fig. 8).

Nevertheless, the possible C source from the carbonated mica schists cannot be excluded, even though carbonates in these rocks show lighter $\delta^{13}C$ values than those in the ophidolomites (Fig. 8). The C isotope compositions can shift toward higher $\delta^{13}C$ values through carbonate reduction (Galvez et al., 2013; Vitale Brovarone et al., 2017). While no reduced C (e.g., graphite and methane) was observed to suggest the significant reduction of the studied ophidolomites, our recent work has recognized abundant abiotic methane-bearing fluid inclusions in several other ophidolomites interpreted to be derived from dolomite reduction

during retrograde serpentinization. Thus, the slightly higher $\delta^{13}C$ values of carbonates in the ophidolomites, compared with those in the carbonated mica schists (Fig. 8), may be ascribed to carbonate reduction. Alternatively, considering the close contact of ophidolomites and carbonated mica schists in the field (Fig. 2b and c), as well as their geochemical similarities (especially Sr isotope compositions; Fig.7a), these rocks may have formed by coupled carbonation along the lithological interface between serpentinites and metasedimentary rocks driven by slab-derived carbonic fluids, in a similar way as recently recognized in Alpine Corsica (Piccoli et al., 2018). The considerably elevated carbonate contents (~30 vol%) and the decreased Sr–C–O isotope compositions (Figs. 7b and 8) of the carbonated mica schists, compared with those of the pristine carbonate-bearing mica schists (~5 vol% carbonate), demonstrate interactions between carbonic fluids and these metasedimentary rocks (Peng et al., 2018). Although detailed carbonation processes especially with respect to the possible C source(s) and quantitative *P–T* conditions of the carbonated metasedimentary rocks remain largely unresolved, the growth of carbonates (dolomite and magnesite) at the expense of phengite (Si = 3.58–3.73 a.p.f.u.) and their association with rutile imply HP carbonation (Peng et al., 2018). Moreover, since equilibrium was likely reached by fluid-mediated reactions particularly at eclogite-facies conditions (e.g., Piccoli et al.,

2016), the aqueous fluids equilibrated with carbonates in the ophidolomites and carbonated mica schists at a temperature of 550 °C (see Section 5.4) display similar $\delta^{18}O$ values of 8.5‰–11.3‰ and 11.0‰–12.5‰, respectively [fractionation factors of $\Delta^{18}O_{dolomite–H_2O}$ and $\Delta^{18}O_{magnesite–H_2O}$ from Zheng (2011) and references therein].

*6.1.2. Fluid-mediated carbonation of serpentinites at high pressures during exhumation*

Due to the dependence of isotopic fractionation on temperature, the elevated $\delta^{18}O$ of carbonates in ophicarbonates from the Mid-Atlantic Ridge (Bonatti et al., 1974) indicates carbonate precipitation during the low-temperature seawater alteration, while those from the Alps and Apennine formed by interactions with seawater at comparatively higher temperatures suggested by their decreasing $\delta^{18}O$ values (Fig. 8; e.g., Barbieri et al., 1979; Schwarzenbach et al., 2013). Thus, the significant $^{18}O$ depletion of carbonates in the studied ophidolomites, similar with that in high-grade (i.e., eclogite-facies) ophicarbonates from the Voltri Massif and Zermatt-Saas, probably reflects the influence of metamorphic fluid–rock interactions at even higher temperatures (Fig. 8; Collins et al., 2015; Scambelluri et al., 2016). Isotope equilibrium temperatures cannot be precisely calculated for the studied ophidolomites, because $\delta^{18}O$ values of silicates equilibrated with carbonates (i.e., coexisting mineral pairs) were not analyzed. Nonetheless, based on O isotope compositions of antigorite

($\delta^{18}O$ = 5.9 ± 0.4‰) in the Tianshan UHP serpentinites (Scicchitano et al., 2018) and dolomite ($\delta^{18}O$ = 10.5 ± 0.2‰) in the studied ophidolomite (Sample C1641) mainly composed of antigorite and dolomite, the equilibrium temperatures of ca. 380–500 °C [fractionation factors of $\Delta^{18}O_{dolomite–calcite}$ from Chacko and Deines (2008) and $\Delta^{18}O_{calcite–serpentine}$ from Zheng (1993)] can be estimated, in overall agreement with the thermodynamically calculated temperatures for the ophidolomites (see Section 5.4).

In comparison with the peak metamorphism of the associated UHP serpentinites ($P$ = 37 ± 7 kbar, $T$ = 510–530 °C), which formed the mineral assemblage Ti-chondrodite + olivine + antigorite + chlorite + magnetite + brucite ± diopside (Shen et al., 2015), the growth of tremolite (having antigorite inclusions; Fig. 4i) in the ophidolomites can be explained by the reaction Atg + Di → Fo + Tr + $H_2O$ at a decreasing pressure but an increasing temperature (Padrón-Navarta et al., 2010, 2012). Besides, since the Al content of antigorite buffered with chlorite is dependent on $P$–$T$ conditions (Padrón-Navarta et al., 2013; Shen et al., 2015), antigorite in the ophidolomites may record the metamorphism from UHP conditions to retrogression as also documented by that in the associated serpentinites (Fig. 6a). Hence, carbonation of these silicates to form ophidolomites postdated the UHP metamorphism of the associated serpentinites but still at relatively high $P$–$T$ conditions as evidenced by

the presence of aragonite and Mg-calcite (Fig. 4d–f; see Section 5.4.2). Furthermore, thermodynamic calculations quantitatively constrained the *P–T* conditions of approximately 15–25 kbar and 550–600 °C for the ophidolomites (Fig. 9 and Supplementary Fig. S2), supporting that they formed by HP carbonation of serpentinites during exhumation of the slab (Fig. 10).

Retrograde fluid production and percolation at *P–T* conditions responsible for the formation of HP ophidolomites are intense in the Tianshan, causing the rehydration of eclogites into blueschists at 15 ± 1 kbar and 580 ± 10 °C (van der Straaten et al., 2008) and the precipitation of rutile and omphacite in retrograde HP veins at 13–21 kbar and 540–580 °C (Lü et al., 2012; Zhang et al., 2016). The common occurrence of carbonates (e.g., dolomite and ankerite) in these rehydrated HP metamafic rocks and retrograde HP veins (van der Straaten et al., 2008, 2012; Lü et al., 2012; Zhang et al., 2016) pronouncedly demonstrates the mobility and precipitation of $CO_2$-bearing fluids at HP conditions during exhumation. The $H_2O$-rich fluids are abundant in the subduction zone from dehydration of sediments, oceanic crust, and serpentinites/ serpentinized slab mantle at high *P–T* conditions (e.g., van der Straaten et al., 2008, 2012; Lü et al., 2012; Zhang et al., 2016; Li et al., 2017). The mobile $H_2O$-rich fluids would drive decarbonation and/or carbonate dissolution (e.g., Frezzotti et al., 2011; Ague and Nicolescu, 2014) in the

carbonate-bearing eclogites and/or carbonated metasedimentary rocks at high *P–T* conditions and thus trigger HP carbonation of serpentinites. Our data demonstrate that relatively lower $X_{CO2}$ values (ca. 0.0005–0.005; Fig. 9 and Supplementary Figs. S1 & S2) in the carbonic fluids will contribute to HP carbonation of serpentinites. This is in accordance with the eclogite-facies carbonation of calcschists (Alpine Corsica) by infiltration of $CO_2$-bearing fluids with $X_{CO2} < 0.005$ (Piccoli et al., 2016), illustrating that aqueous fluids characterized by low $X_{CO2}$ can cause HP carbonation of subduction-zone rocks.

To further evaluate the possible role of carbonate-bearing eclogites as the C source responsible for the formation of ophidolomites, we calculated the composition and speciation of fluids in equilibrium with both rock types (Fig. 11; see Section 4.7.2 for calculation details) under variable *P–T* conditions along the retrograde path of the Tianshan (red arrow line in Fig. 10; Zhang et al., 2018). At temperatures of 600–400 °C along this *P–T* path, fluids in equilibrium with carbonate-bearing eclogite contain substantially higher total dissolved C concentration than those in equilibrium with ophidolomite (Fig. 11a and c). The most important C-bearing aqueous species in the fluids equilibrated with carbonate-bearing eclogite at these conditions are $CO_{2,aq}$, $NaHCO_{3,aq}$, and $HCO_3^-$ (Fig. 11d). Because bulk Na and K contents are very low in ophidolomite and corresponding phases (e.g., phlogopite) were not observed, these

elements were not considered in calculations for the ophidolomite (Fig. 11a and b). However, test calculations predicted the stability of Na-phlogopite in the presence of Na in ophidolomite and a very high (> 1 molal) concentration of $NaHCO_{3,aq}$ in the fluids. This indicates that $NaHCO_{3,aq}$, $HCO_3^-$, and $Na^+$ in the fluids infiltrated into ophidolomite will remain highly soluble and are thus not expected to participate directly in the precipitation of carbonate minerals. Hence, the difference of $CO_{2,aq}$ concentrations in the fluids equilibrated with carbonate-bearing eclogite and ophidolomite is the main driving force for carbonate precipitation. At the *P–T* conditions proposed for the formation of ophidolomites in the Tianshan (grey fields in Fig. 11; see also Section 5.4), fluids emanating from carbonate-bearing eclogite have a $CO_{2,aq}$ concentration of up to 1.9 molal, considerably higher than that in the fluids equilibrated with ophidolomite (Fig. 11b and d). Based on the difference of $CO_{2,aq}$ concentrations and the estimated $CO_2$ content of ophidolomite (~2.53 wt%; Table 5), the formation of 1 kg of ophidolomite would require an infiltration of ~0.3 kg fluid derived from carbonate-bearing eclogite. Moreover, $HCOO^-$, metal-formate complexes (e.g., $FeHCOO^+$ and $CaHCOO^+$), and methane may also contribute to C release from carbonate-bearing eclogite and carbonate precipitation in ophidolomite (Fig. 11b and d). However, their concentrations in the fluids equilibrated with ophidolomite are somewhat uncertain because the

controlling factors such as the oxygen fugacity and redox equilibria between solids and fluids (Tumiati and Malaspina, 2018) are not well constrained in this rock (see Section 4.7.2). In addition to C and Na, fluids derived from carbonate-bearing eclogite may also have transferred minor amounts of Si, Al, and Fe to the ophidolomite (Fig. 11a and c).

### *6.2. Ophimagnesites and listvenites: reactivation of $CO_2$-bearing fluids during late exhumation*

Listvenites represent interactions of ultramafic rocks with $CO_2$-bearing fluids along faults, shear zones, or other tectonic contacts that can provide paths for the infiltrated fluids (Qiu and Zhu, 2018 and references therein). Listvenites at Changawuzi commonly enclose unreacted serpentinites in the field (Fig. 2d) and they are mostly composed of carbonates (magnesite and dolomite), quartz, and fuchsite (Fig. 5e and f; Table 1), indicating the complete carbonation of serpentinites (i.e., listvenitization). Besides, ophimagnesites (i.e., partly listvenitized serpentinites in this study) also occur in contact with these listvenite blocks (Fig. 2d). The lithological sequence of serpentinites–ophimagnesites–listvenites records the stepwise carbonation of serpentinites by infiltration of $CO_2$-bearing fluids (e.g., Klein and Garrido, 2011; Menzel et al., 2018). Therefore, the field occurrence suggests that the studied ophimagnesites and listvenites shared the mutual C source(s), as indicated by their similar carbonate compositions (Fig. 6b) and isotopic signatures (Figs. 7b and 8). However,

whether or not listvenites can form is largely dependent on the $X_{CO2}$ in the infiltrated carbonic fluids—a low $X_{CO2}$ (~$10^{-4}$–$10^{-3}$) for the stability of ophimagnesites while a comparatively higher $X_{CO2}$ (~$10^{-2}$) for listvenites under *P*–*T* conditions of 2–3 kbar and 300 °C (e.g., Menzel et al., 2018).

Microstructural relationships (Fig. 5a–d) and mineral compositions (e.g., $X_{Mg}$ values; see Section 5.1) indicate that carbonates in the ophimagnesites and listvenites were derived from interactions of chrysotile, antigorite, and talc with $CO_2$-bearing fluids. Carbonates in the ophimagnesites and listvenites show C–O isotope compositions distinct from those in both marine-originated (e.g., Bonatti et al., 1974; Barbieri et al., 1979; Schwarzenbach et al., 2013) and high-grade (Collins et al., 2015; Scambelluri et al., 2016; this study) carbonated serpentinites, but similar to those in low-grade carbonated serpentinites from the Bracco unit (Italy), the Mt. Figogna unit (Italy), and the Ubaye Valley (France) in the Western Alps (Fig. 8; Collins et al., 2015). Compared with the relatively uniform $\delta^{13}C$, however, carbonates in the ophimagnesites and listvenites exhibit a wide range of $\delta^{18}O$. This C–O isotopic trend is similar to that of carbonates in metasomatic marbles from Alpine Corsica (Piccoli et al., 2016), which was interpreted as evidence for carbonation (i.e., interactions of Ca- and/or Mg-rich silicates with $CO_2$-bearing fluids). Compared with the serpentinites, the considerably elevated initial $^{87}Sr/^{86}Sr$ ratios of most ophimagnesites and listvenites provide evidence

for the possible C source from the carbonate-bearing mica schists (Fig. 7b; Peng et al., 2018). However, few ophimagnesites and listvenites show lower Sr–C–O isotope compositions, indicating a possible contribution of C from the associated carbonated mica schists (Figs. 7b and 8; Peng et al., 2018). Hence, the isotopic evidence suggests that the $CO_2$-bearing fluids responsible for the formation of ophimagnesites and listvenites may largely stem from the associated metasedimentary rocks, as supported by the close contact of these lithologies in the field (Fig. 2d). Furthermore, potassium (K) metasomatism is a unique feature of the listvenitization reflected by the ubiquitous K-rich minerals (e.g., fuchsite) in the listvenites (Fig. 5e and f; e.g., Halls and Zhao, 1995), providing compelling evidence for the origin of metasomatic $CO_2$-bearing fluids from the metasedimentary rocks.

Obtaining precise *P–T* constraints for the ophimagnesites and listvenites by thermodynamic modelling is difficult due to the insensitivity of their mineral assemblages to *P–T* conditions. Listvenites can form at relatively low temperatures of 80–130 °C (Falk and Kelemen, 2015) and under (sub)greenschist-facies conditions of ca. 1–3 kbar and 250–350 °C (e.g., Halls and Zhao, 1995; Zoheir and Lehmann, 2011; Beinlich et al., 2012; Menzel et al., 2018). Associated with the higher-temperature listvenites, several lithological zones composed of distinctive mineral assemblages (serpentine ± magnesite, magnesite + talc, and

magnesite + quartz) are commonly predicted to record the stepwise carbonation reactions of serpentinites (Menzel et al., 2018 and references therein). Accordingly, the studied ophimagnesites (antigorite + magnesite ± talc ± dolomite ± chrysotile) and listvenites (magnesite + quartz + fuchsite ± dolomite ± chlorite) most probably represent the stepwise carbonation of serpentinites under (sub)greenschist-facies conditions. As a result, interactions between $CO_2$-bearing fluids and serpentinites to form LP ophimagnesites and listvenites during late exhumation illustrate the fluid-mediated reactive carbonation of subduction-zone serpentinites at relatively shallow crustal levels (Fig. 10).

### *6.3. Implications for the deep C cycle*

Carbonation of serpentinites and serpentinized oceanic lithospheric mantle at mid-ocean ridges and slab flexures to form pristine ophicarbonates has been highlighted because of the potential contribution to the subduction influx of C (e.g., Dasgupta and Hirschmann, 2010; Alt et al., 2012, 2013). Subduction of the pristine ophicarbonates can regulate the distribution of C between shallow and deep reservoirs by (1) triggering C mobilization by infiltration of $H_2$-rich fluids (Vitale Brovarone et al., 2017), and (2) recycling C into the deep mantle in the absence of the reduced fluids (e.g., Kerrick and Connolly, 1998; Menzel et al., 2019). Furthermore, carbonation of the hydrated mantle wedge (e.g., Falk and Kelemen, 2015; Kelemen and Manning, 2015; Menzel et

al., 2018; Sieber et al., 2018) and subduction-zone serpentinites (Scambelluri et al., 2016; Piccoli et al., 2018) also has important implications for the deep Earth C cycle (Sieber et al., 2018).

While HP carbonation of serpentinites in our case study took place during exhumation of the slab, the *P–T* estimates (ca. 15–25 kbar and 550–600 °C; see Section 5.4) are analogous to the modeled prograde *P–T* paths of subduction zones (Gerya et al., 2002; Syracuse et al., 2010; Penniston-Dorland et al., 2015) and similar to those of subducted HP ophicarbonates (*P* = 20–25 kbar, *T* = 500–600 °C) from comparable metamorphic settings (Fig. 10; Scambelluri et al., 2016). Hence, the HP carbonation processes described here may yield insights into C retention in subducted serpentinites from the downgoing slabs and subduction mélanges (Spandler et al., 2008; Scambelluri et al., 2016), and thus provide large-scale implications for the deep C cycle (Fig. 12). The $H_2O$-rich fluids released from dehydration of subducted sediments, oceanic crust, and serpentinites/serpentinized slab mantle at high *P–T* conditions induce C mobilization in subducted carbonate-bearing reservoirs (e.g., Frezzotti et al., 2011; Ague and Nicolescu, 2014). Enhanced infiltration of the reactive $CO_2$-bearing aqueous fluids ($X_{CO2}$ ~ $10^{-4}$–$10^{-3}$) into subducted serpentinites at a depth of ca. 70 km (Scambelluri et al., 2016; Piccoli et al., 2018; this study) would result in HP fluid–rock interactions, through which carbonates are precipitated mainly by replacing silicates

(e.g., antigorite, olivine, clinopyroxene, and tremolite). Channelized fluid flow along subduction shear zones or lithological boundaries (e.g., Angiboust et al., 2011, 2014; Piccoli et al., 2016, 2018) may cause the intense percolation of carbonic fluids parallel to the downgoing plates and facilitate HP carbonation of subducted serpentinites. In this scenario, the formation of HP ophicarbonates is likely associated with the coupled HP carbonation of the overlying metasedimentary rocks at the lithological interfaces, similar to the observations from lawsonite-eclogite units in Alpine Corsica (Piccoli et al., 2018). Thus, subducted serpentinites can efficiently sequestrate slab-derived C at HP conditions. Furthermore, the investigated lower-grade ophimagnesites and listvenites imply that hydrated ultramafic rocks in subducted slabs can also be served as highly effective reactants to sequestrate slab-originated C even at relatively shallow crustal levels. As a result, the multistage $CO_2$ sequestration in subducted serpentinites over a wide range of *P–T* conditions may potentially influence the evaluation of C fluxes in subduction zones. Although substantial quantities of slab-derived C could be captured and stored in the overlying plates (Kelemen and Manning, 2015), the increasingly recognized carbonation of various lithologies within subduction zones, including ultramafic rocks (Scambelluri et al., 2016; Piccoli et al., 2018; this study), mafic rocks (van der Straaten et al., 2008, 2012; Piccoli et al., 2018), and sedimentary rocks (Piccoli et al., 2016,

2018; Peng et al., 2018) may potentially recycle subducted C into the deep mantle and exert an important control on the C distribution between shallow and deep reservoirs.

The typical ophidolomite (C1518, ~5 vol% carbonate) and listvenite (C1541-1, ~60 vol% carbonate) were used to evaluate the C sequestration potential of serpentinites at both HP and LP conditions. Adopting densities of 2.98 g/cm$^3$ for magnesite, 2.86 g/cm$^3$ for dolomite, 2.60 g/cm$^3$ for antigorite, 2.60–3.30 g/cm$^3$ for chlorite, 2.65 g/cm$^3$ for quartz, and 2.77–2.88 g/cm$^3$ for fuchsite (replaced by muscovite; Deer et al., 1992), densities of about 2.61–3.17 g/cm$^3$ and 2.82–2.83 g/cm$^3$ were calculated for the ophidolomite and listvenite, respectively. The $CO_2$ contents are ~2.53 wt% for the ophidolomite and ~30.32 wt% for the listvenite (Table 5), calculated based on mineral compositions and modes of carbonates in these samples (Table 5; see also Section 5.4). These estimates are plausible since they are similar to the $CO_2$ contents of HP ophidolomites ($CO_2$ = 3 wt%) from the Ligurian Alps (Scambelluri et al., 2016) and LP listvenites ($CO_2$ = 30 wt%) from the Samail ophiolite (Falk and Kelemen, 2015). On the basis of the estimated densities and $CO_2$ contents, about 18–22 Mt and 233–234 Mt C could be captured and stored in per km$^3$ of precursor serpentinites forming HP ophidolomites and LP listvenites, respectively. This confirms the outstanding C storage potential of serpentinites at both HP and LP conditions (e.g., Power et al.,

2013; Scambelluri et al., 2016).

## 7. Conclusions

Two carbonation processes of subduction-zone serpentinites, which happened at different stages of exhumation from HP conditions to relatively shallow crustal levels in the Chinese southwestern Tianshan HP–UHP metamorphic belt, provide important implications for C sequestration within subducted lithologies and potentially influence the global estimates of C fluxes at convergent margins. The integrated field occurrence, microstructures, Sr–C–O isotope compositions, and thermodynamic modelling elucidate that the growth of carbonates in the HP ophidolomites is attributed to interactions between serpentinites and $CO_2$-bearing aqueous fluids from carbonate-bearing eclogites and/or carbonated mica schists at ca. 15–25 kbar and 550–600 °C. Alternatively, ophidolomites and carbonated mica schists may have formed by coupled HP carbonation along the lithological interface between serpentinites and metasedimentary rocks driven by slab-derived carbonic fluids. Subsequent fluid–rock interactions at relatively shallow crustal levels resulted in a second stage of serpentinite carbonation to form LP ophimagnesites and listvenites, during which the potential C source may have originated from metasedimentary rocks. Estimates indicate that ~20 Mt C and ~230 Mt C could be captured and stored in per $km^3$ of

precursor subduction-zone serpentinites forming HP ophidolomites and LP listvenites, respectively. Thus, carbonation of subducted serpentinites may exert an important control on C distribution between shallow and deep reservoirs.

**Acknowledgements**

This work was financially supported by The National Natural Science Foundation of China (41520104004, 41330210, and 41872067) and The National Basic Research Program of China (2015CB856105). The first author is deeply indebted to an invitation from Stefano Poli and a scholarship from Graduate School of Peking University (2018-02-005) for supporting his PhD study in Italy. We are grateful to Thomas Bader, Ryosuke Oyanagi, José Alberto Padrón-Navarta, and Zhou Tan for helpful discussions. We thank Zhicheng Liu and Yang Wang for their help during fieldwork. We also thank Hongrui Ding, Wennian Han, Xiangtian Jin, Xiaoli Li, Dongdong Ma, Fang Ma, Hong Qin, Zhaofeng Zhang, Hongli Zhu, and Wenping Zhu for their patient assistance during sample analyses. The authors wish to acknowledge Esther Schwarzenbach, Melanie Sieber, and an anonymous reviewer for their detailed and constructive comments that substantially helped to improve the manuscript. Wolfgang Bach is greatly appreciated for his editorial handling and helpful suggestions.

**References**


Ague J. J. and Nicolescu S. (2014) Carbon dioxide released from subduction zones by fluid-mediated reactions. *Nat. Geosci.* **7**, 355–360.

Alt J. C., Garrido C. J., Shanks W. C., Turchyn A., Padrón-Navarta J. A., López Sánchez-Vizcaíno V., Gómez-Pugnaire, M. T. and Marchesi C. (2012) Recycling of water, carbon, and sulfur during subduction of serpentinites: a stable isotope study of Cerro del Almirez, Spain. *Earth Planet. Sci. Lett.* **327–328**, 50–60.

Alt J. C., Schwarzenbach E. M., Früh-Green G. L., Shanks W. C., Bernasconi S. M., Garrido C. J., Crispini L., Gaggero L., Padrón-Navarta J. A. and Marchesi C. (2013) The role of serpentinites in cycling of carbon and sulfur: seafloor serpentinization and subduction metamorphism. *Lithos* **178**, 40–54.

Angiboust S., Agard P., Raimbourg H., Yamato P. and Huet B. (2011) Subduction interface processes recorded by eclogite-facies shear zones (Monviso, W. Alps). *Lithos* **127**, 222–238.

Angiboust S., Pettke T., de Hoog J. C. M., Caron B. and Oncken O. (2014) Channelized fluid flow and eclogite-facies metasomatism along the subduction shear zone. *J. Petrol.* **55**, 883–916.

Anovitz L. M. and Essene E. J. (1987) Phase equilibria in the system $CaCO_3$–$MgCO_3$–$FeCO_3$. *J. Petrol.* **28,** 389–414.

Bach W. and Früh-Green G. L. (2010) Alteration of the oceanic lithosphere and implications for seafloor processes. *Elements* **6**, 173–178.

Bach W., Rosner M., Jöns N., Rausch S., Robinson L. F., Paulick H. and Erzinger J. (2011) Carbonate veins trace seawater circulation during

exhumation and uplift of mantle rock: Results from ODP Leg 209. *Earth Planet. Sci. Lett.* **311**, 242–252.

Barbieri M., Masi U. and Tolomeo L. (1979) Stable isotope evidence for a marine origin of ophicalcites from the North-Central Apennine (Italy). *Mar. Geol.* **30**, 193–204.

Beinlich A., Klemd R., John T. and Gao J. (2010) Trace-element mobilization during Ca metasomatism along a major fluid conduit: eclogitization of blueschist as a consequence of fluid-rock interaction. *Geochim. Cosmochim. Acta* **74**, 1892–1922.

Beinlich A., Plümper O., Hövelmann J., Austrheim H. and Jamtveit B. (2012) Massive serpentinite carbonation at Linnajavri, N-Norway. *Terra Nova* **24**, 446–455.

Berner R. A. (1999) A new look at the long-term carbon cycle. *GSA Today* **9**, 1–6.

Bonatti E., Emiliani C., Ferrera G., Honnorez J. and Rydell H. (1974) Ultramafic-carbonate breccias from the equatorial Mid Atlantic Ridge. *Mar. Geol.* **16**, 83–102.

Boschi C., Dini A., Früh-Green G. L. and Kelley D. S. (2008) Isotope and element exchange during serpentinization and metasomatism at the Atlantis Massif (MAR 30°N): insights from B and Sr isotope data. *Geochim. Cosmochim. Acta* **72**, 1801–1823.

Cannat M., Lagabrielle Y., Bougault H., Casey J., de Coutures N., Dmitriev L. and Fouquet Y. (1997) Ultramafic and gabbroic exposures at the Mid-Atlantic Ridge: geological mapping in the 15°N region. *Tectonophysics* **279**, 193–213.

Chacko T. and Deines P. (2008) Theoretical calculation of oxygen isotope fractionation factors in carbonate systems. *Geochim. Cosmochim. Acta* **72**, 3642–3660.

Clerc C., Boulvais P., Lagabrielle Y. and de Saint Blanquat M. (2014) Ophicalcites from the northern Pyrenean belt: a field, petrographic and stable isotope study. *Int. J. Earth Sci.* **103**, 141–163.

Collins N. C., Bebout G. E., Angiboust S., Agard P., Scambelluri M., Crispini L. and John T. (2015) Subduction-zone metamorphic pathway for deep carbon cycling: II. Evidence from HP/UHP metabasaltic rocks and ophicarbonates. *Chem. Geol.* **412**, 132–150.

Connolly J. A. D. (2005) Computation of phase equilibria by linear programming: a tool for geodynamic modelling and its application to subduction zone decarbonation. *Earth Planet. Sci. Lett.* **236**, 524–541.

Connolly J. A. D. and Galvez M. E. (2018) Electrolytic fluid speciation by Gibbs energy minimization and implications for subduction zone mass transfer. *Earth Planet. Sci. Lett.* **501,** 90–102.

Dasgupta R. and Hirschmann M. M. (2010) The deep carbon cycle and melting in Earth's interior. *Earth Planet. Sci. Lett.* **298**, 1–13.

Deer W. A., Howie R. A. and Zussman J. (1992) *An introduction to the rock-forming minerals, 2nd edition.* Mineralogical Society, London, UK.

Delacour A., Früh-Green G. L., Frank M., Gutjahr M. and Kelley D. S. (2008) Sr-and Nd-isotope geochemistry of the Atlantis Massif (30°N, MAR): implications for fluid fluxes and lithospheric heterogeneity. *Chem. Geol.* **254**, 19–35.

Dvir O., Pettke T., Fumagalli P. and Kessel R. (2011) Fluids in the peridotite–water system up to 6 GPa and 800°C: new experimental constrains on dehydration reactions. *Contrib. Mineral. Petrol.* **161**, 829–844.

Edwards H. G. M., Jorge Villar S. E., Jehlicka J. and Munshi T. (2005) FT–Raman spectroscopic study of calcium-rich and magnesium-rich carbonate minerals. *Spectrochim. Acta* **61**, 2273–2280.

Falk E. S. and Kelemen P. B. (2015) Geochemistry and petrology of listvenite in the Samail ophiolite, Sultanate of Oman: Complete carbonation of peridotite during ophiolite emplacement. *Geochim. Cosmochim. Acta* **160**, 70–90.

Frezzotti M. L., Selverstone J., Sharp Z. D. and Compagnoni R. (2011) Carbonate dissolution during subduction revealed by diamond-bearing rocks from the Alps. *Nat. Geosci.* **4**, 703–706.

Früh-Green G. L., Kelley D. S., Bernasconi S. M., Karson J. A., Ludwig K. A., Butterfield D. A., Boschi C. and Proskurowski G. (2003) 30000 years of hydrothermal activity at the Lost City vent field. *Nature* **301**, 495–498.

Früh-Green G. L., Orcutt B. N., Rouméjon S., Lilley M. D., Morono Y., Cotterill C., Green S., Escartin J., John B. E., McCaig A. M., Cannat M., Ménez B., Schwarzenbach E. M., Williams M. J., Morgan S., Lang S. Q., Schrenk M. O., Brazelton W. J., Akizawa N., Boschi C., Dunkel K. G., Quéméneur M., Whattam S. A., Mayhew L., Harris M., Bayrakci G., Behrmann J-H., Herrero-Bervera E., Hesse K., Liu H-Q., Ratnayake A. S., Twing K., Weis D., Zhao R. and Bilenker L. (2018) Magmatism, serpentinization and life: Insights through drilling the Atlantis Massif (IODP Expedition 357). *Lithos* **323**, 137–155.

Galvez M. E., Manning C. E., Connolly J. A. D. and Rumble D. (2015) The solubility of rocks in metamorphic fluids: A model for rock-dominated conditions to upper mantle pressure and temperature. *Earth Planet. Sci. Lett.* **430**, 486–498.

Galvez M. E., Martinez I., Beyssac O., Benzerara K., Agrinier P. and Assayag N. (2013) Metasomatism and graphite formation at a lithological interface in Malaspina (Alpine Corsica, France). *Contrib. Mineral. Petrol.* **166**, 1687–1708.

Gao J. and Klemd R. (2001) Primary fluids entrapped at blueschist to

eclogite transition: evidence from Tianshan meta-subduction complex in northwestern China. *Contrib. Mineral. Petrol.* **142**, 1–14.

Gao J., John T., Klemd R. and Xiong X. (2007) Mobilization of Ti–Nb–Ta during subduction: evidence from rutile-bearing dehydration segregations and veins hosted in eclogite, Tianshan, NW China. *Geochim. Cosmochim. Acta* **71**, 4974–4996.

Gerya T. V., Stöckhert B. and Perchuk A. L. (2002) Exhumation of high-pressure metamorphic rocks in a subduction channel: a numerical simulation. *Tectonics* **21**. https://doi.org/10.1029/2002TC001406.

Goldsmith J. R. and Newton R. C. (1969) P–T–X relations in the system $CaCO_3$–$MgCO_3$ at high temperatures and pressures. *Am. J. Sci.* **267**, 160–190.

Gorman P. J., Kerrick D. M. and Connolly J. A. D. (2006) Modelling open system metamorphic decarbonation of subducting slabs. *Geochem. Geophys. Geosyst.* **7**. https://doi.org/10.1029/2005GC001125.

Halls C. and Zhao R. (1995) Listvenite and related rocks: perspectives on terminology and mineralogy with reference to an occurrence at Cregganbaun, Co., Mayo, Republic of Ireland. *Mineral. Deposita* **30**, 303–313.

Hansen L. D., Dipple G. M., Gordon T. M. and Kellett D. A. (2005) Carbonated serpentinite (listwanite) at Atlin, British Columbia: a geological analogue to carbon dioxide sequestration. *Can. Mineral.* **43**, 225–239.

Hermann J., Troitzsch U. and Scott D. (2016) Experimental subsolidus phase relations in the system $CaCO_3$–$CaMg(CO_3)_2$ up to 6.5 GPa and implications for subducted marbles. *Contrib. Mineral. Petrol.* **171**. https://doi.org/10.1007/s00410-016-1296-y.

Hoefs J. (2009) *Stable Isotope Geochemistry, 6th edition*. Springer.

Verlag Berlin Heidelberg.

Holland T. and Powell R. (1991) A Compensated-Redlich-Kwong (CORK) equation for volumes and fugacities of $CO_2$ and $H_2O$ in the range 1 bar to 50 kbar and 100–1600°C. *Contrib. Mineral. Petrol.* **109**, 265–273.

Holland T. J. B. and Powell R. (1998) An internally consistent thermodynamic data set for phases of petrological interest. *J. Metamorph. Geol.* **16**, 309–343.

Huang F. and Sverjensky D. A. (2019) Extended Deep Earth Water model for predicting major element mantle metasomatism. *Geochim. Cosmochim. Acta* **254**, 192–230.

Jarrard R. D. (2003) Subduction fluxes of water, carbon dioxide, chlorine, and potassium. *Geochem. Geophys. Geosyst.* **4**, 8905.

John T., Klemd R., Gao J. and Garbe-Schönberg C. D. (2008) Trace-element mobilization in slabs due to non steady-state fluid–rock interaction: constraints from an eclogite-facies transport vein in blueschist (Tianshan, China). *Lithos* **103**, 1–24.

Kelemen P. B. and Manning C. E. (2015) Reevaluating carbon fluxes in subduction zones, what goes down, mostly comes up. *Proc. Natl. Acad. Sci. USA* **112**, E3997–E4006.

Kelley D. S., Karson J. A., Früh-Green G. L., Yoerger D. R., Shank T. M., Butterfield D. A., Hayes J. M., Schrenk M. O., Olson E. J., Proskurowski G., Jakuba M., Bradley A., Larson B., Ludwig K., Glickson D., Buckman K., Bradley A. S., Brazelton W. J., Roe K., Elend M. J., Delacour A., Bernasconi S. M., Lilley M. D., Baross J. A., Summons R. E. and Sylva S. P. (2005) A serpentinite-hosted ecosystem: the Lost City hydrothermal field. *Science* **307**, 1428–1434.

Kerrick D. M. and Connolly J. A. D. (1998) Subduction of ophicarbonates and recycling of $CO_2$ and $H_2O$. *Geology* **26**, 375–378.

Kerrick D. M. and Connolly J. A. D. (2001a) Metamorphic devolatilization of subducted oceanic metabasalts: implications for seismicity, arc magmatism and volatile recycling. *Earth Planet. Sci. Lett.* **189**, 19–29.

Kerrick D. M. and Connolly J. A. D. (2001b) Metamorphic devolatilization of subducted marine sediments and the transport of volatiles into the Earth's mantle. *Nature* **411**, 293–296.

Klein F. and Garrido C. J. (2011) Thermodynamic constraints on mineral carbonation of serpentinized peridotite. *Lithos* **126**, 147–160.

Lafay R., Baumgartner L. P., Stephane S., Suzanne P., German M. H. and Torsten V. (2017). Petrologic and stable isotopic studies of a fossil hydrothermal system in ultramafic environment (Chenaillet ophicalcites, Western Alps, France): Processes of carbonate cementation. *Lithos* **294–295**, 319–338.

Li J.-L., Gao J., John T., Klemd R. and Su W. (2013) Fluid-mediated metal transport in subduction zones and its link to arc-related giant ore deposits: constraints from a sulfide-bearing HP vein in lawsonite eclogite (Tianshan, China). *Geochim. Cosmochim. Acta* **120**, 326–362.

Li J.-L., John T., Gao J., Klemd R. and Wang X.-S. (2017) Subduction channel fluid–rock interaction and mass transfer: Constraints from a retrograde vein in blueschist (SW Tianshan, China). *Chem. Geol.* **456**, 28–42.

Li J.-L., Klemd R., Gao J. and Meyer M. (2012) Coexisting carbonate-bearing eclogite and blueschist in SW Tianshan, China: Petrology and phase equilibria. *J. Asian Earth Sci.* **60**, 174–187.

Li J.-L., Klemd R., Gao J. and Meyer M. (2014) Compositional zoning in dolomite from lawsonite-bearing eclogite (SW Tianshan, China): Evidence for prograde metamorphism during subduction of oceanic crust. *Am. Mineral.* **99**, 206–217.

Li X.-P., Zhang L., Wei C., Ai Y. and Chen J. (2007) Petrology of rodingite derived from eclogite in western Tianshan, China. *J. Metamorph. Geol.* **25**, 363–382.

Li X., Zhang L., Wei C., Slabunov A. I. and Bader T. (2018) Quartz and orthopyroxene exsolution lamellae in clinopyroxene and the metamorphic P–T path of Belomorian eclogites. *J. Metamorph. Geol.* **36,** 1–22.

Li X.-P., Zhang L.-F., Wilde S. A., Song B. and Liu X.-M. (2010) Zircons from rodingite in the Western Tianshan serpentinite complex: mineral chemistry and U–Pb ages define nature and timing of rodingitization. *Lithos* **118**, 17–34.

Liou J. G., Tsujimori T., Zhang R. Y., Katayama I. and Maruyama S. (2004) Global UHP metamorphism and continental subduction/ collision: the Himalayan model. *Int. Geol. Rev.* **46**, 1–27.

Lü Z., Zhang L., Du J., Yang X., Tian Z. and Xia B. (2012) Petrology of HP metamorphic veins in coesite-bearing eclogite from western Tianshan, China: fluid processes and elemental mobility during exhumation in a cold subduction zone. *Lithos* **136–139**, 168–186.

Manning C. E. (2014) A piece of the deep carbon puzzle. *Nat. Geosci.* **7**, 333–334.

Menzel M. D., Garrido C. J., López Sánchez-Vizcaíno V., Hidas K. and Marchesi C. (2019) Subduction metamorphism of serpentinite-hosted carbonates beyond antigorite-serpentinite dehydration (Nevado-Filábride Complex, Spain). *J. Metamorph. Geol.* **37**, 681–715.

Menzel M. D., Garrido C. J., López Sánchez-Vizcaíno V., Marchesi C., Hidas K., Escayola M. P. and Delgado-Huertas A. (2018) Carbonation of mantle peridotite by $CO_2$-rich fluids: the formation of listvenites in the Advocate ophiolite complex (Newfoundland, Canada). *Lithos* **323**, 238–261.

Molina J. F. and Poli S. (2000) Carbonate stability and fluid composition in subducted oceanic crust: an experimental study on $H_2O$–$CO_2$-bearing basalts. *Earth Planet. Sci. Lett.* **176**, 295–310.

Mposkos E., Baziotis I., Proyer A. and Hoinkes G. (2006) Dolomitic marbles from the ultrahigh-pressure metamorphic Kimi complex in Rhodope, N.E. Greece. *Mineral. Petrol.* **88**, 341–362.

Padrón-Navarta J. A., Hermann J., Garrido C. J., López Sánchez-Vizcaíno V. and Gómez-Pugnaire, M. T. (2010) An experimental investigation of antigorite dehydration in natural silica-enriched serpentinite. *Contrib. Mineral. Petrol.* **159**, 25–42.

Padrón-Navarta J. A., López Sánchez-Vizcaíno V., Hermann J., Connolly J. A. D., Garrido C. J., Gómez-Pugnaire, M. T. and Marchesi C. (2013) Tschermak's substitution in antigorite and consequences for phase relations and water liberation in high-grade serpentinites. *Lithos* **178**, 186–196.

Padrón-Navarta J. A., Tommasi A., Garrido C. J. and López Sánchez-Vizcaíno V. (2012) Plastic deformation and development of antigorite crystal preferred orientation in high-pressure serpentinites. *Earth Planet. Sci. Lett.* **349–350**, 75–86.

Peng W., Zhang L., Shen T. and Hu H. (2018) Implications for the deep carbon cycle from the carbonation in subduction zones: A case study of carbonated micaschists from Chinese southwestern Tianshan. *Acta Petrol. Sin.* **34**, 1204–1218.

Penniston-Dorland S. C., Kohn M. J. and Manning C. E. (2015) The global range of subduction zone thermal structures from exhumed blueschists and eclogites: rocks are hotter than models. *Earth Planet. Sci. Lett.* **428**, 243–254.

Piccoli F., Vitale Brovarone A. and Ague J. J. (2018) Field and petrological study of metasomatism and high-pressure carbonation

from lawsonite eclogite-facies terrains, Alpine Corsica. *Lithos* **304–307**, 16–37.

Piccoli F., Vitale Brovarone A., Beyssac O., Martinez I., Ague J. J. and Chaduteau C. (2016) Carbonation by fluid–rock interactions at high-pressure conditions: implications for carbon cycling in subduction zones. *Earth Planet. Sci. Lett.* **445**, 146–159.

Plank T. and Langmuir C. H. (1998) The chemical composition of subducting sediment and its consequences for the crust and mantle. *Chem. Geol.* **145**, 325–394.

Power I. M., Wilson S. A. and Dipple G. M. (2013) Serpentinite carbonation for $CO_2$ sequestration. *Elements* **9**, 115–121.

Qiu T. and Zhu Y. (2018) Listwaenite in the Sartohay ophiolitic mélanges (Xinjiang, China): A genetic model based on petrology, U-Pb chronology and trace element geochemistry. *Lithos* **302–303**, 427–446.

Rinaudo C., Gastaldi D. and Belluso E. (2003) Characterization of chrysotile, antigorite and lizardite by FT-Raman spectroscopy. *Can. Mineral.* **41**, 883–890.

Scambelluri M., Bebout G. E., Belmonte D., Gilio M., Campomenosi N., Collins N. and Crispini L. (2016) Carbonation of subduction-zone serpentinite (high-pressure ophicarbonate; Ligurian Western Alps) and implications for the deep carbon cycling. *Earth Planet. Sci. Lett.* **441**, 155–166.

Schwarzenbach E. M., Früh-Green G. L., Bernasconi S. M., Alt J. C. and Plas A. (2013) Serpentinization and carbon sequestration: A study of two ancient peridotite-hosted hydrothermal systems. *Chem. Geol.* **351**, 115–133.

Scicchitano M. R., Rubatto D., Hermann J., Shen T., Padrón-Navarta J. A., Williams I. S. and Zheng Y.-F. (2018) *In situ* oxygen isotope

determination in serpentine minerals by ion microprobe: reference materials and applications to ultrahigh-pressure serpentinites. *Geostand. Geoanal. Res.* **42**, 459–479.

Shen T., Hermann J., Zhang L., Lü Z., Padrón-Navarta J. A., Xia B. and Bader T. (2015) UHP metamorphism documented in Ti-chondrodite- and Ti-clinohumite-bearing serpentinized ultramafic rocks from Chinese southwestern Tianshan. *J. Petrol.* **56**, 1425–1458.

Shen T., Wu F., Zhang L., Hermann J., Li X. and Du J. (2016) In-situ U–Pb dating and Nd isotopic analysis of perovskite from a rodingite blackwall associated with UHP serpentinite from southwestern Tianshan, China. *Chem. Geol.* **431**, 67–82.

Sieber M. J., Hermann J. and Yaxley G. M. (2018) An experimental investigation of C–O–H fluid-driven carbonation of serpentinites under forearc conditions. *Earth Planet. Sci. Lett.* **496**, 178–188.

Song S., Su L., Li X. H., Zhang G., Niu Y. and Zhang L. (2010) Tracing the 850-Ma continental flood basalts from a piece of subducted continental crust in the North Qaidam UHPM belt, NW China. *Precambrian Res.* **183**, 805–816.

Spandler C., Hermann J., Faure K., Mavrogenes J. A. and Arculus R. J. (2008) The importance of talc and chlorite “hybrid” rocks for volatile recycling through subduction zones; evidence from the high-pressure subduction mélange of New Caledonia. *Contrib. Mineral. Petrol.* **155**, 181–198.

Syracuse E. M., van Keken P. E. and Abers G. A. (2010) The global range of subduction zone thermal models. *Phys. Earth Planet. In.* **183**, 73–90.

Tan Z., Agard P., Gao J., John T., Li J., Jiang T., Bayet L., Wang X. and Zhang X. (2017) P–T–time-isotopic evolution of coesite-bearing eclogites: Implications for exhumation processes in SW Tianshan.

*Lithos* **278–281**, 1–25.

Tao R., Zhang L., Li S., Zhu J. and Ke S. (2018) Significant contrast in the Mg–C–O isotopes of carbonate between carbonated eclogite and marble from the S.W. Tianshan UHP subduction zone: Evidence for two sources of recycled carbon. *Chem. Geol.* **483**, 65–77.

Thomsen T. B. and Schmidt M. W. (2008) Melting of carbonated pelites at 2.5–5.0 GPa, silicate–carbonatite liquid immiscibility, and potassium–carbon metasomatism of the mantle. *Earth Planet. Sci. Lett.* **267**, 17–31.

Tian Z. L. and Wei C. J. (2013) Metamorphism of ultrahigh-pressure eclogites from the Kebuerte Valley, South Tianshan, NW China: phase equilibria and PT path. *J. Metamorph. Geol.* **31**, 281–300.

Tsuno K. and Dasgupta R. (2011) Melting phase relation of nominally anhydrous, carbonated pelitic-eclogite at 2.5–3.0 GPa and deep cycling of sedimentary carbon. *Contrib. Mineral. Petrol.* **161**, 743–763.

Tumiati S. and Malaspina N. (2018) Redox processes and the role of carbon-bearing volatiles from the slab–mantle interface to the mantle wedge. *J. Geol. Soc.* **176**, 388–397.

van der Straaten F., Halama R., John T., Schenk V., Hauff F. and Andersen N. (2012) Tracing the effects of high-pressure metasomatic fluids and seawater alteration in blueschist facies overprinted eclogites: implications for subduction channel processes. *Chem. Geol.* **292–293**, 69–87.

van der Straaten F., Schenk V., John T. and Gao J. (2008) Blueschist-facies rehydration of eclogites (Tian Shan, NW–China): implications for fluid–rock interaction in the subduction channel. *Chem. Geol.* **255**, 195–219.

Veizer J., Ala D., Azmy K., Bruckschen P., Buhl D., Bruhn F., Carden G.

A. F., Diener A., Ebneth S., Godderis Y., Jasper T., Korte C., Pawellek F., Podlaha O. G. and Strauss H. (1999) $^{87}Sr/^{86}Sr$, $\delta^{13}C$ and $\delta^{18}O$ evolution of Phanerozoic seawater. *Chem. Geol.* **161**, 59–88.

Vitale Brovarone A., Martinez I., Elmaleh A., Compagnoni R., Chaduteau C., Ferraris C. and Esteve I. (2017) Massive production of abiotic methane during subduction evidenced in metamorphosed ophicarbonates from the Italian Alps. *Nat. Commun.* **8**, 14134.

Whitney D. L. and Evans B. W. (2010) Abbreviations for names of rock-forming minerals. *Am. Mineral.* **95**, 185–187.

Xia B., Zhang L., Xia Y. and Bader T. (2014) The tectonic evolution of the Tianshan Orogenic Belt: Evidence from U–Pb dating of detrital zircons from the Chinese southwestern Tianshan accretionary mélange. *Gondwana Res.* **25**, 1627–1643.

Zhang L., Du J., Lü Z., Yang X., Gou L., Xia B., Chen Z., Wei C. and Song S. (2013) A huge oceanic-type UHP metamorphic belt in southwestern Tianshan, China: peak metamorphic age and P–T path. *Chinese Sci. Bull.* **58**, 4378–4383.

Zhang L., Wang Y., Zhang L. and Lü Z. (2018) Ultrahigh pressure metamorphism and tectonic evolution of southwestern Tianshan orogenic belt, China: a comprehensive review. *Geol. Soc. Spec. Publ.* **474**,133–152.

Zhang L., Zhang L., Lü Z., Bader T. and Chen Z. (2016) Nb–Ta mobility and fractionation during exhumation of UHP eclogite from southwestern Tianshan, China. *J. Asian Earth Sci.* **122**, 136–157.

Zheng Y.-F. (1993) Calculation of oxygen isotope fractionation in hydroxyl-bearing silicates. *Earth Planet. Sci. Lett.* **120**, 247–263.

Zheng Y.-F. (2011) On the theoretical calculations of oxygen isotope fractionation factors for carbonate-water systems. *Geochem. J.* **45**, 341–354.

Zhu J., Zhang L., Lü Z. and Bader T. (2018) Elemental and isotopic (C, O, Sr, Nd) compositions of Late Paleozoic carbonated eclogite and marble from the SW Tianshan UHP belt, NW China: Implications for deep carbon cycle. *J. Asian Earth Sci.* **153**, 307–324.

Zoheir B. and Lehmann B. (2011) Listvenite–lode association at the Barramiya gold mine, Eastern Desert, Egypt. *Ore Geol. Rev.* **39**, 101–115.

**Figure captions**

Fig. 1. Geological background of the study area. (a) Simplified tectonic framework of the western part of Chinese Tianshan (modified from Tian and Wei, 2013). (b) Schematic geological map of the Chinese southwestern Tianshan HP–UHP metamorphic belt (modified from Zhang et al., 2013). (c) Detailed geological map of the study area showing distribution of sample locations (modified from Shen et al., 2015).

Fig. 2. General field features of the study area. (a) Large serpentinite blocks are enclosed in carbonate-bearing mica schists and carbonated mica schists, with carbonated serpentinites sampled in these blocks. (b–c) Ophidolomites are located at the top of serpentinites and are closely associated with (retrograde) eclogites and carbonated mica schists. (d) Listvenites show close contact with carbonate-bearing mica schists and enclose relict serpentinites and ophimagnesites.

Fig. 3. Representative textures of carbonated serpentinites from the study area. (a) Ophidolomite showing euhedral to subhedral dolomite grains evenly distributed in the host serpentinite. (b) Ophidolomite showing dolomite veins cutting across the host serpentinite, with dolomite grains visible. (c) Ophimagnesite displaying the host serpentinite filled by

magnesite grains and irregular veins. (d) Listvenite having a yellowish weathered surface but a greenish fresh surface caused by fuchsite (Cr-rich mica). Mineral abbreviations in this study are after Whitney and Evans (2010).

Fig. 4. Petrographic characteristics of representative ophidolomites from the study area. (a–b) Euhedral to subhedral dolomite grains (having ilmenite inclusions) in the matrix of antigorite and chlorite. (c) Antigorite, chlorite, and diopside enclosed in ilmenite. (d) Carbonate phases growing at the expense of diopside (having antigorite inclusions) in the matrix of antigorite and chlorite. (e) The Mg compositional mapping of the box in (d), highlighting the color difference of dolomite, aragonite, and Mg-calcite. (f) The Raman spectrum of aragonite in (e), with typical bands of aragonite denoted. (g) Dolomite vein growing after antigorite. (h) Dolomite replacing tremolite in the matrix of antigorite. (i) Relict antigorite enclosed in the dolomitized tremolite.

Fig. 5. Petrographic characteristics of representative ophimagnesites and listvenites from the study area. (a) Late magnesite-bearing chrysotile veins cutting across the host serpentinite. (b) The Raman spectrum of chrysotile in (a), with typical bands of chrysotile denoted. (c–d) Ophimagnesites comprising euhedral to subhedral magnesite grains in the matrix of antigorite, with or without talc. Magnesite commonly contains inclusions of former antigorite. (e–f) Listvenites consisting of magnesite, quartz, and green fuchsite, with or without dolomite. Fuchsite is related to the decomposition of chromite and suffers later chloritization. The left and right parts of (f) are shown under plane-polarized and cross-polarized light, respectively.

Fig. 6. Compositions of major rock-forming minerals in carbonated serpentinites from the study area. (a) Al (a.p.f.u.) *vs.* Si (a.p.f.u.) of antigorite in ophidolomites and ophimagnesites. For comparison, low-Al UHP antigorite and high-Al retrograde antigorite in the associated serpentinites (Shen et al., 2015) are also plotted. (b) Ternary $CaCO_3$–$MgCO_3$–$FeCO_3$ compositional plots of carbonates in ophidolomites, ophimagnesites, and listvenites.

Fig. 7. (a) Initial $^{87}Sr/^{86}Sr$ ratios ($t$ = 320 Ma) *vs.* Sr contents of serpentinites, ophidolomites, and the carbonate separates from the study area. Data of carbonate-bearing eclogites (van der Straaten et al., 2012) and carbonated mica schists (Peng et al., 2018) from Tianshan are also plotted. Sr isotope compositions of Ordovician–Carboniferous seawater (green hatched areas) are taken from Veizer et al. (1999) while those of marine-originated ophicarbonates from the Apennine and of carbonates in ophicarbonates from the Mid-Atlantic Ridge are from Barbieri et al. (1979) and Bonatti et al. (1974), respectively. (b) Initial $^{87}Sr/^{86}Sr$ ratios ($t$ = 290 Ma) *vs.* $\delta^{13}C_{V\text{-}PDB}$ values of serpentinites, ophimagnesites, listvenites, and the carbonate separates from the study area. Data of carbonate-bearing mica schists and carbonated mica schists (Peng et al., 2018) from Tianshan are also plotted. Uncertainties of the isotope values are smaller than the symbol size.

Fig. 8. C and O isotope compositions of carbonates in carbonated serpentinites from the study area (modified from Clerc et al., 2014). The light green area shows the $\delta^{13}C$ range of marine carbonates (Hoefs, 2009). C and O isotope values of carbonates in carbonate-bearing eclogites (Collins et al., 2015; Zhu et al., 2018), carbonate-bearing mica schists (Peng et al., 2018), and carbonated mica schists (Peng et al., 2018)

from Tianshan are also plotted. $\delta^{13}C$ and $\delta^{18}O$ of carbonates in ophicarbonates from the Mid-Atlantic Ridge are taken from Bonatti et al. (1974), while those in high-grade ophicarbonates from the Voltri Massif and Zermatt-Saas and in low-grade ophicarbonates from Bracco, Mt. Figogna, and Ubaye are from Collins et al. (2015). For comparison, $\delta^{13}C$ and $\delta^{18}O$ ranges of carbonates in high-temperature ophicarbonates, Alpine and Apenninic ophicarbonates, and low-temperature ophicarbonates (seawater related) are also shown (following Clerc et al., 2014). Uncertainties of the isotope values are smaller than the symbol size.

Fig. 9. Phase diagrams calculated in the CFMASH–$CO_2$ system for HP ophidolomites from the study area. (a) *P–T* pseudosection for homogeneous ophidolomite C1518 based on the effective bulk composition. Isopleths of the Al content of antigorite ($y_{Atg}$ = Al/8 in a.p.f.u., blue dotted line; Padrón-Navarta et al., 2013), mineral modes of olivine (vol%, green stippled line), and $X_{CO2}$ in fluids (red stippled line) are contoured in the pseudosection. (b) *P–T* pseudosection for inhomogeneous ophidolomite C1531-2 based on the local composition. The aragonite–Mg-calcite transition (pink solid line) was experimentally determined by Hermann et al. (2016).

Fig. 10. Schematic illustration showing two carbonation processes of serpentinites at different stages of exhumation from HP conditions to relatively shallow crustal levels in the Chinese southwestern Tianshan. The thermobaric conditions responsible for the formation of listvenites are from Halls and Zhao (1995). *P–T* estimates of UHP serpentinites from Tianshan (Shen et al., 2015) and subducted HP ophicarbonates from the Ligurian Alps (Scambelluri et al., 2016) are also shown for comparison.

The pink (Tan et al., 2017) and red (Zhang et al., 2018) arrow lines display the *P–T* trajectories of the Chinese southwestern Tianshan. Facies boundaries and abbreviations are from Liou et al. (2004).

Fig. 11. The composition and speciation of fluids in equilibrium with (a and b) ophidolomite and (c and d) carbonate-bearing eclogite under variable *P–T* conditions along the retrograde path of the Chinese southwestern Tianshan (red arrow line in Fig. 10; Zhang et al., 2018). (a) Total element concentration dissolved and (b) C-bearing aqueous species in fluids equilibrated with ophidolomite (C1518) in the Ca–Fe–Mg–Al–Si–C–O–H system. Mineral assemblage: (1) Atg Chl Ol Mgs Cpx. Note that the small differences in phase stabilities compared with the *P–T* pseudosection (Fig. 9a) are due to the different fluid solution models and redox conditions. (c) Total element concentration dissolved and (d) C-bearing aqueous species in fluids equilibrated with carbonate-bearing eclogite from Tianshan (Sample L0910 from Li et al., 2014) in the Na–Ca–K–Fe–Mg–Al–Si–C–O–H system. Mineral assemblages: (2) Ep Fsp Mica Cal Omph Amph Chl, (3) Ep Fsp Mica Cal Omph Amph Chl Q, (4) Ep Mica Cal Omph Amph Chl Q, (5) Ep Mica Dol Omph Amph Q, (6) Ep Mica Dol Omph Amph Q Grt, and (7) Ep Mica Dol Mgs Omph Q Grt. At the *P–T* conditions constrained for the ophidolomite formation (grey fields), fluids from carbonate-bearing eclogite contain significantly higher $CO_2$ than those from ophidolomite.

Fig. 12. A general model for HP carbonation of hydrated ultramafic rocks in subduction zones (modified from Piccoli et al., 2018; see text for detailed explanations). It is possible that the coupled HP carbonation of the overlying metasedimentary rocks (with or without carbonates) along the lithological interfaces forms carbonated metasedimentary rocks

(Piccoli et al., 2016, 2018; this study). The upper left figure illustrates the potential regions of serpentinite carbonation in the hydrated mantle wedge and within the subducted slab (modified from Sieber et al., 2018), in which the maximum depth of antigorite stability is from Angiboust et al. (2014). Both figures are not to scale.

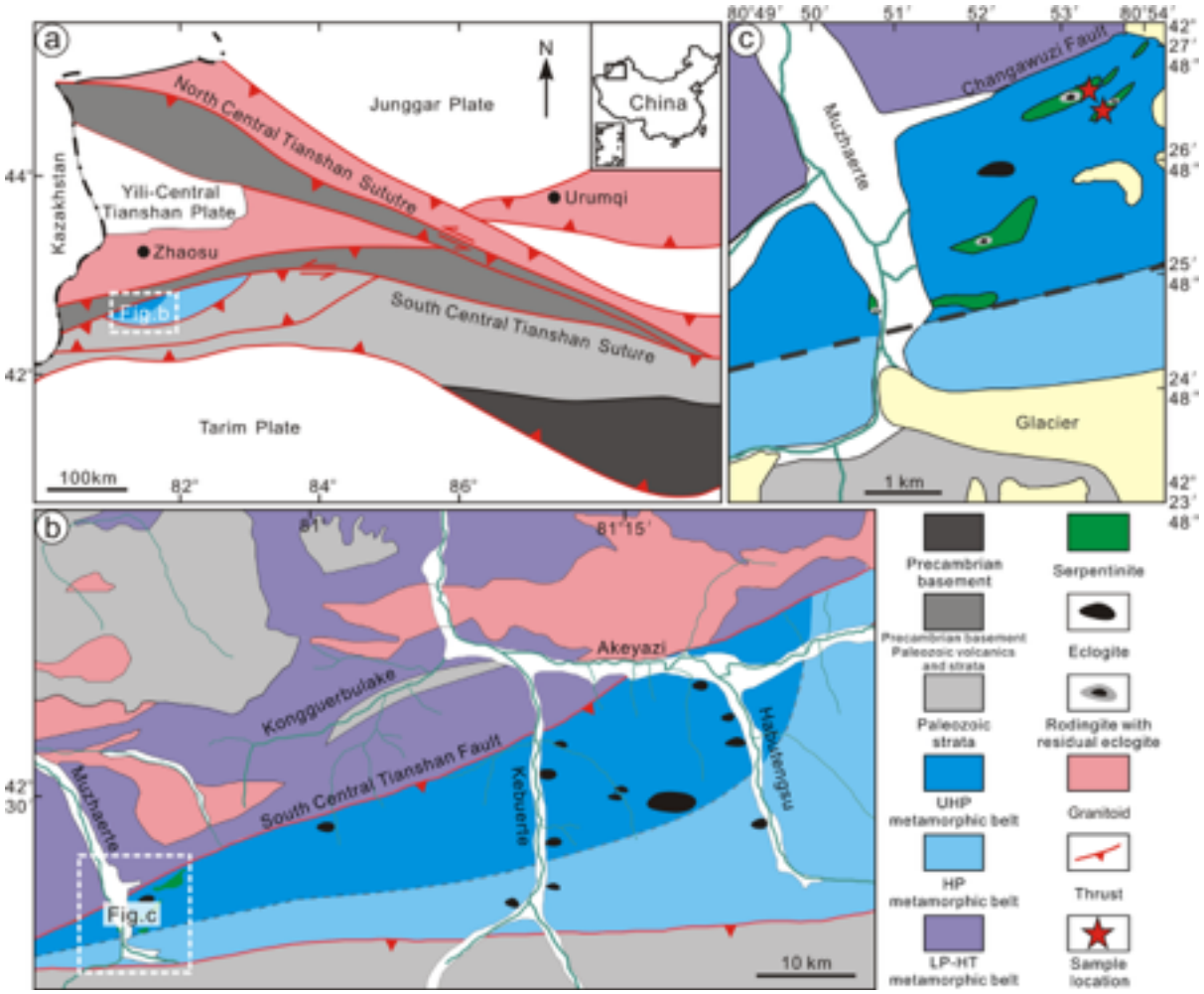
a
N
China
Junggar Plate
North Central Tianshan Sututre
Urumqi
Yili-Central
Tianshan Plate
Zhaosu
Kazakhstan
Fig.b
South Central Tianshan Suture
Tarim Plate
100km
82°
84°
86°
44°
42°
b
81°
81°15′
Akeyazi
Kongguerbulake
South Central Tianshan Fault
Muzhaerte
Kebuerte
Habutengsu
Fig.c
42°
30′
10 km
c
80°49′
50′
51′
52′
53′
80°54′
Changawuzi Fault
Muzhaerte
Glacier
1 km
42°
27′
48″
26′
48″
25′
48″
24′
48″
42°
23′
48″
Precambrian basement
Precambrian basement Paleozoic volcanics and strata
Paleozoic strata
UHP metamorphic belt
HP metamorphic belt
LP-HT metamorphic belt
Serpentinite
Eclogite
Rodingite with residual eclogite
Granitoid
Thrust
Sample location

**Figure 1**

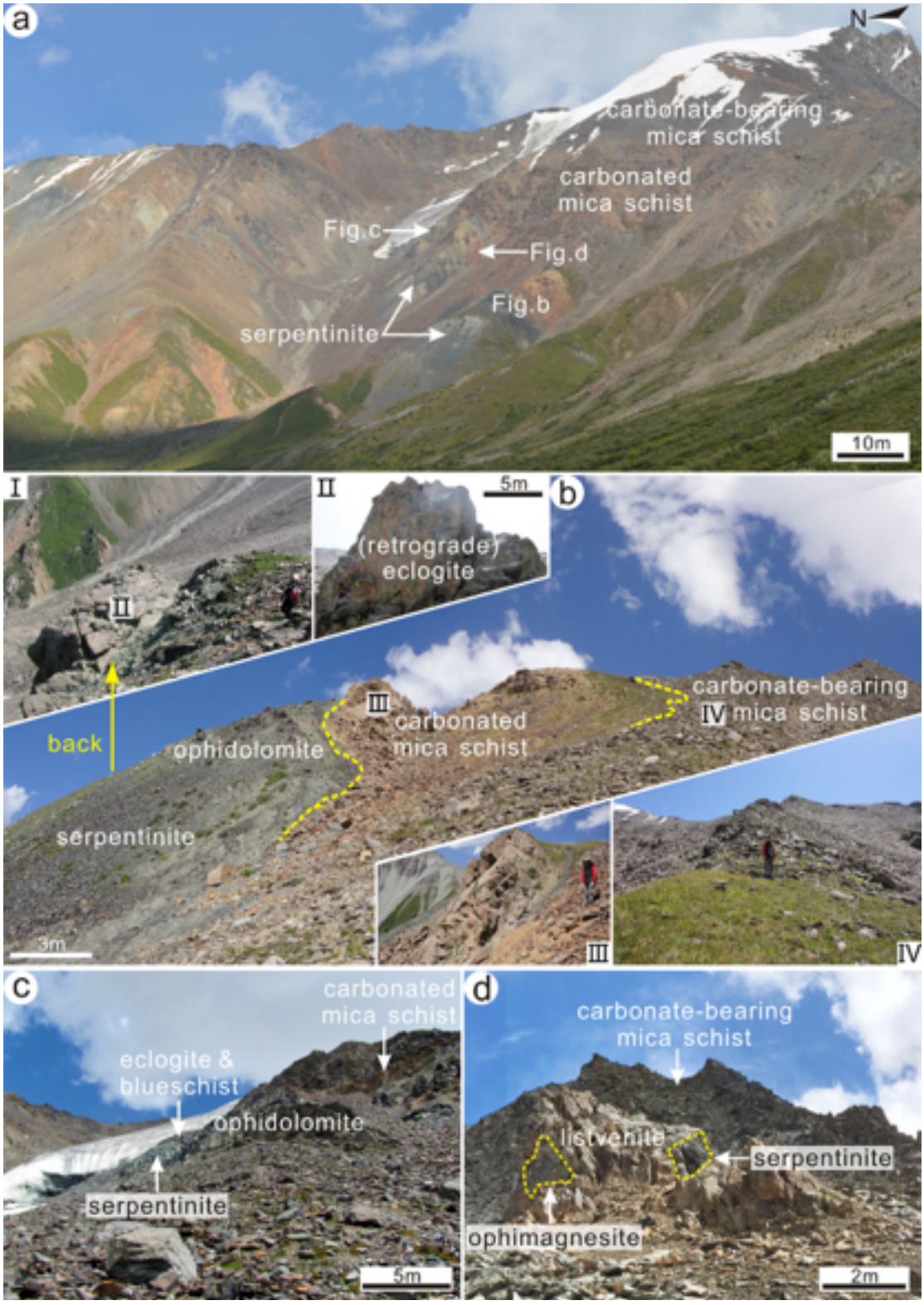
a
N
carbonate-bearing
mica schist
carbonated
mica schist
Fig.c
Fig.d
Fig.b
serpentinite
10m
I
II
5m
(retrograde)
eclogite
b
back
ophidolomite
III
carbonated
mica schist
carbonate-bearing
IV mica schist
serpentinite
3m
III
IV
c
carbonated
mica schist
eclogite &
blueschist
ophidolomite
serpentinite
5m
d
carbonate-bearing
mica schist
listvenite
serpentinite
ophimagnesite
2m

**Figure 2**

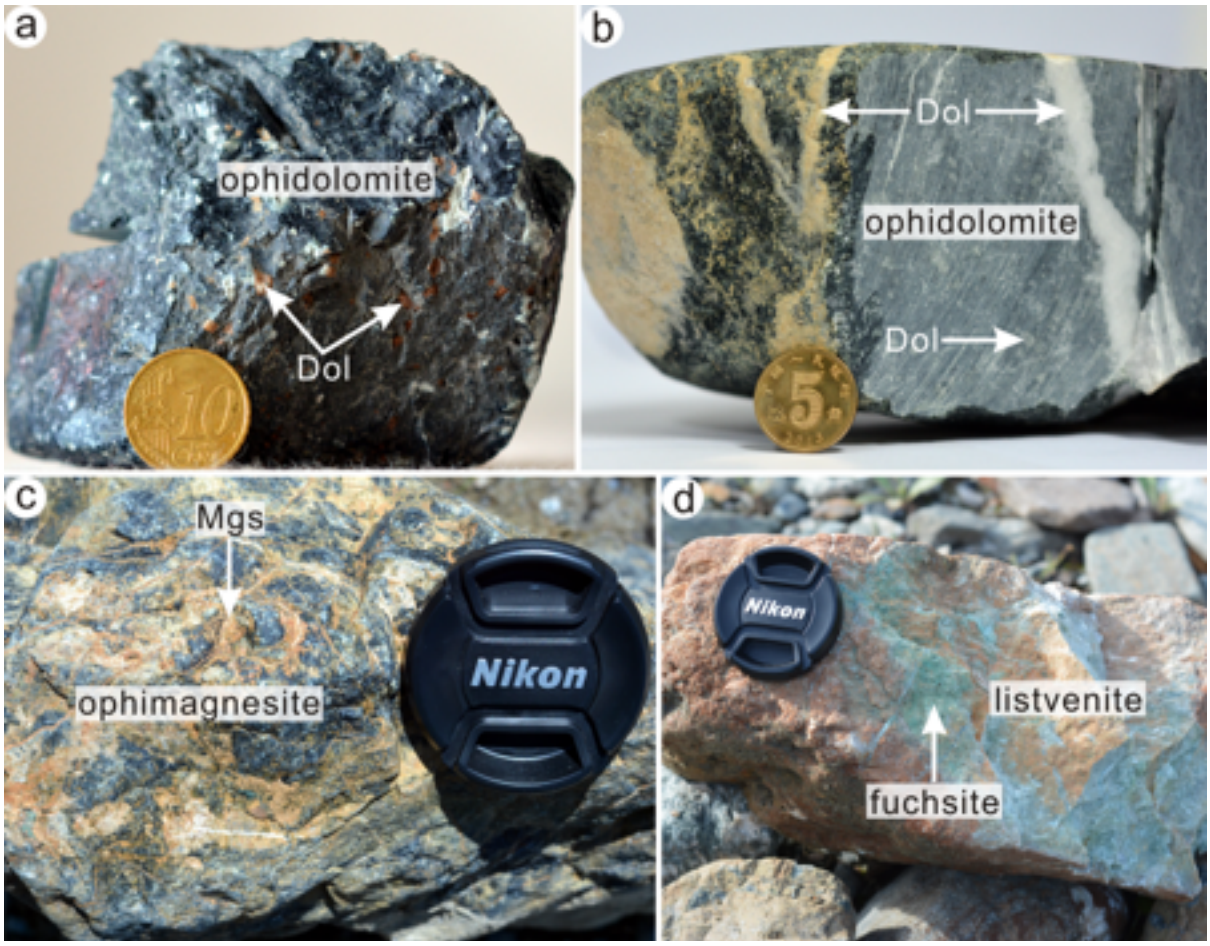
a
ophidolomite
Dol
b
Dol
ophidolomite
Dol
c
Mgs
ophimagnesite
Nikon
d
Nikon
listvenite
fuchsite

**Figure 3**

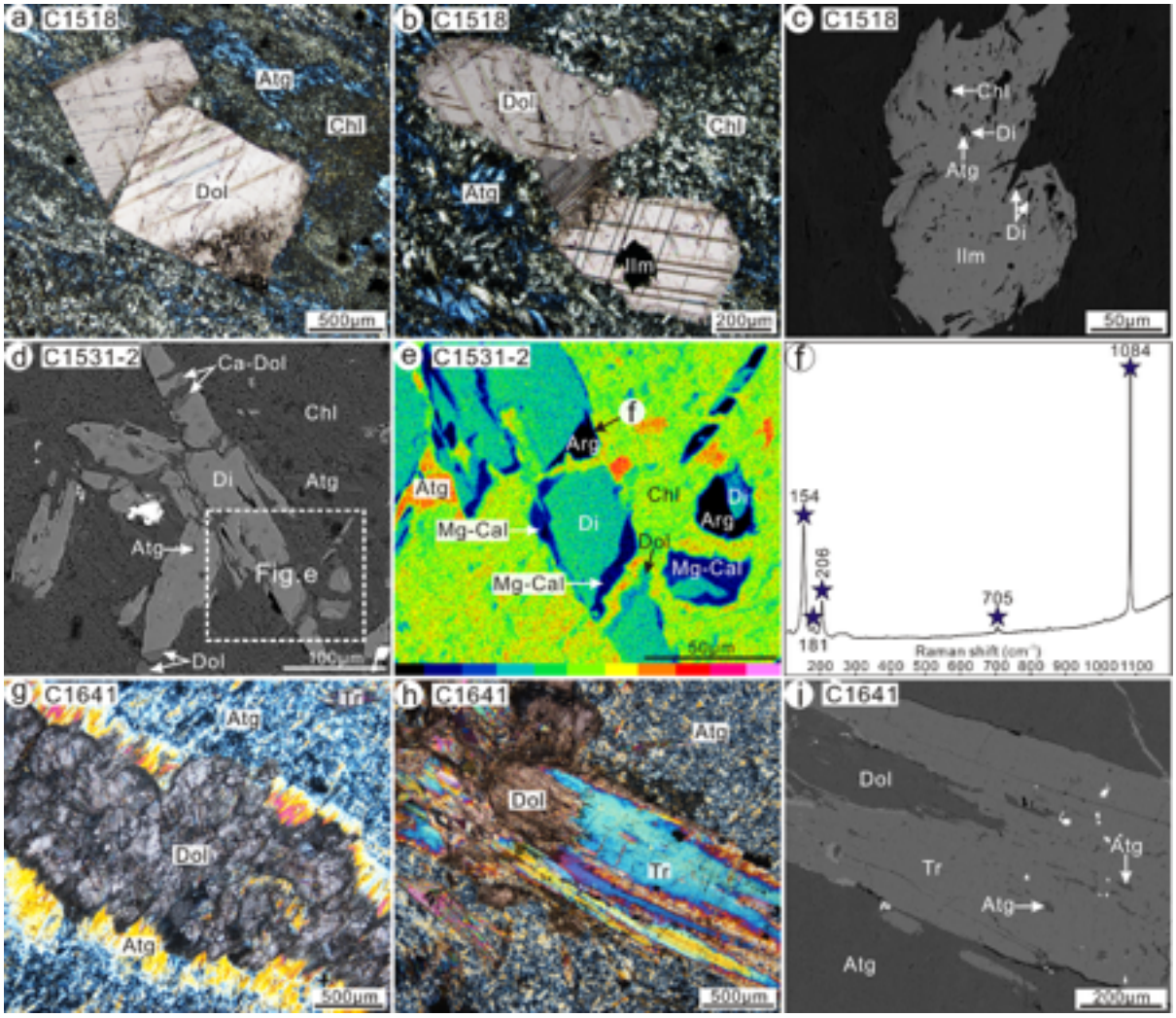
a C1518
Atg
Chl
Dol
500μm
b C1518
Dol
Chl
Atg
Ilm
200μm
c C1518
Chl
Di
Atg
Di
Ilm
50μm
d C1531-2
Ca-Dol
Chl
Di
Atg
Atg
Fig.e
Dol
100μm
e C1531-2
f
Arg
Atg
Chl
Di
Mg-Cal
Di
Dol
Arg
Mg-Cal
Mg-Cal
50μm
f
1084
154
206
705
181
Raman shift (cm⁻¹)
200 300 400 500 600 700 800 900 1000 1100
g C1641
Atg
Tr
Dol
Atg
500μm
h C1641
Atg
Dol
Tr
500μm
i C1641
Dol
Atg
Tr
Atg
Atg
200μm

**Figure 4**

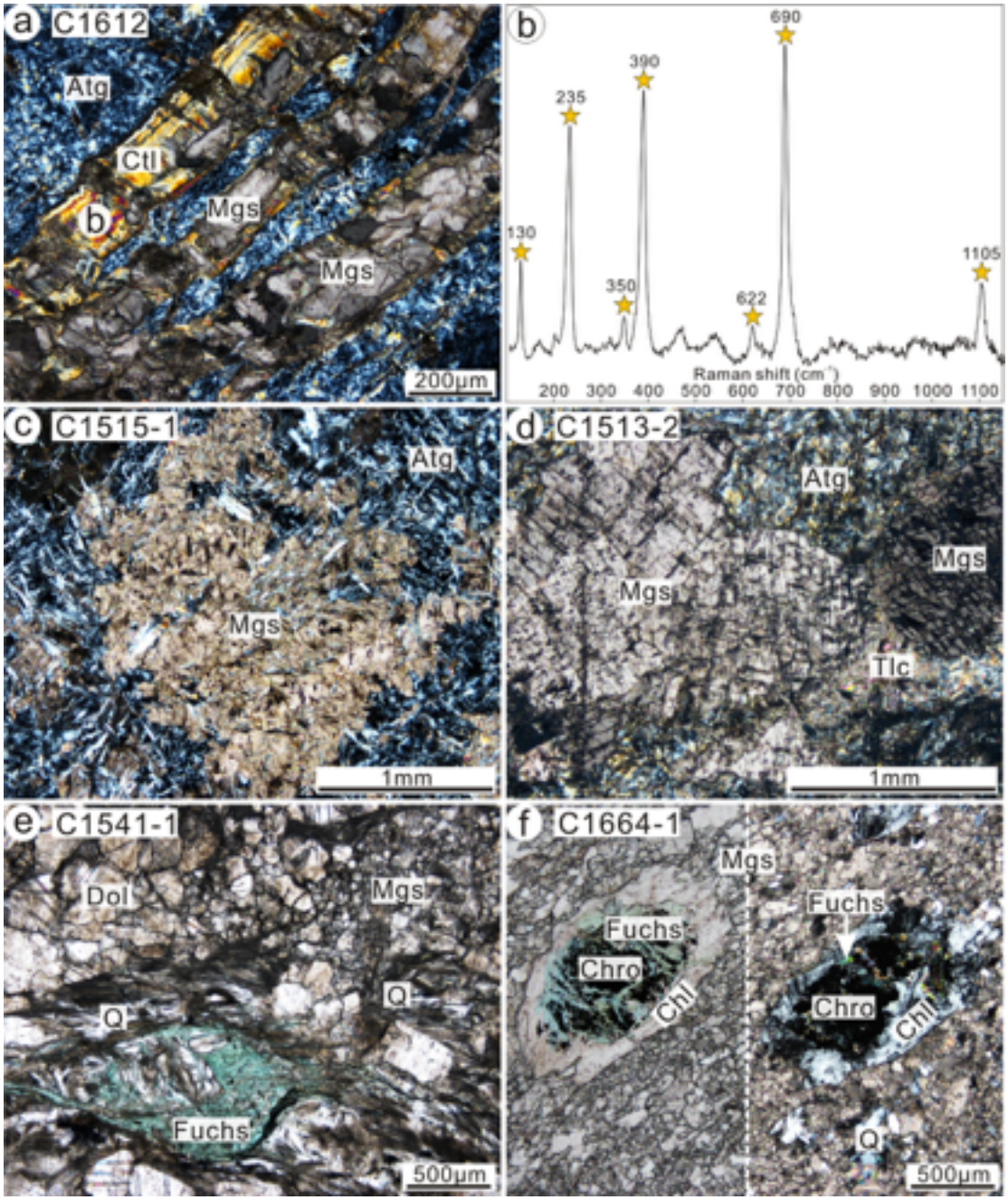
a C1612
Atg
Ctl
b
Mgs
Mgs
200μm
b
690
390
235
130
350
622
1105
Raman shift (cm⁻¹)
200 300 400 500 600 700 800 900 1000 1100
c C1515-1
Atg
Mgs
1mm
d C1513-2
Atg
Mgs
Mgs
Tlc
1mm
e C1541-1
Dol
Mgs
Q
Q
Fuchs
500μm
f C1664-1
Mgs
Fuchs
Chro
Chl
Fuchs
Chro
Chl
Q
500μm

**Figure 5**

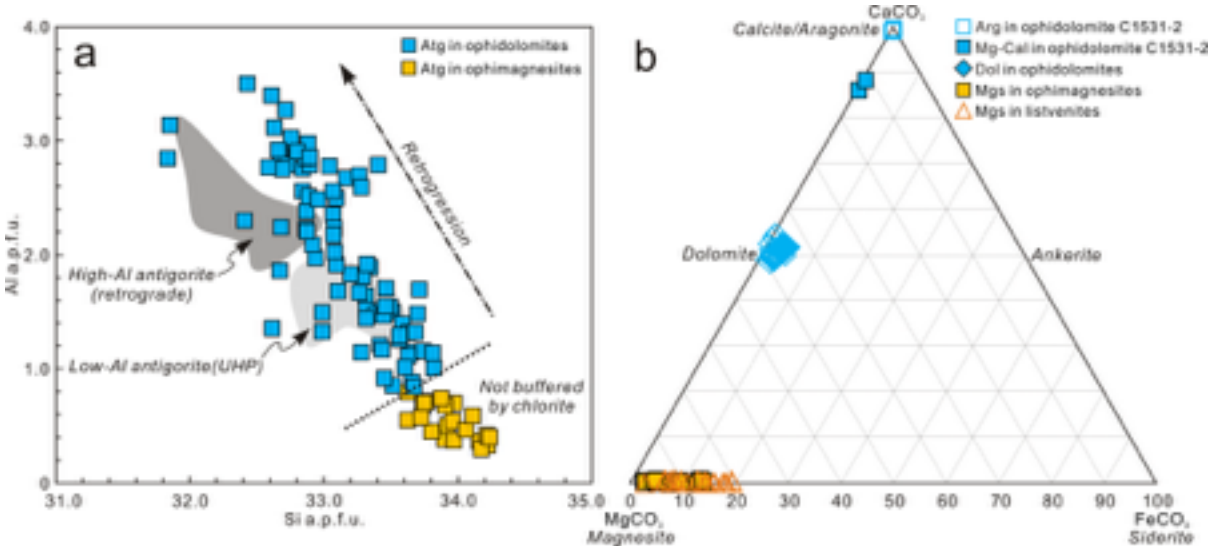
a
Atg in ophidolomites
Atg in ophimagnesites
Retrogression
High-Al antigorite (retrograde)
Low-Al antigorite(UHP)
Not buffered by chlorite
Al a.p.f.u.
Si a.p.f.u.
4.0
3.0
2.0
1.0
0
31.0
32.0
33.0
34.0
35.0
b
CaCO3
Calcite/Aragonite
Arg in ophidolomite C1531-2
Mg-Cal in ophidolomite C1531-2
Dol in ophidolomites
Mgs in ophimagnesites
Mgs in listvenites
Dolomite
Ankerite
MgCO3
Magnesite
FeCO3
Siderite
0
10
20
30
40
50
60
70
80
90
100

**Figure 6**

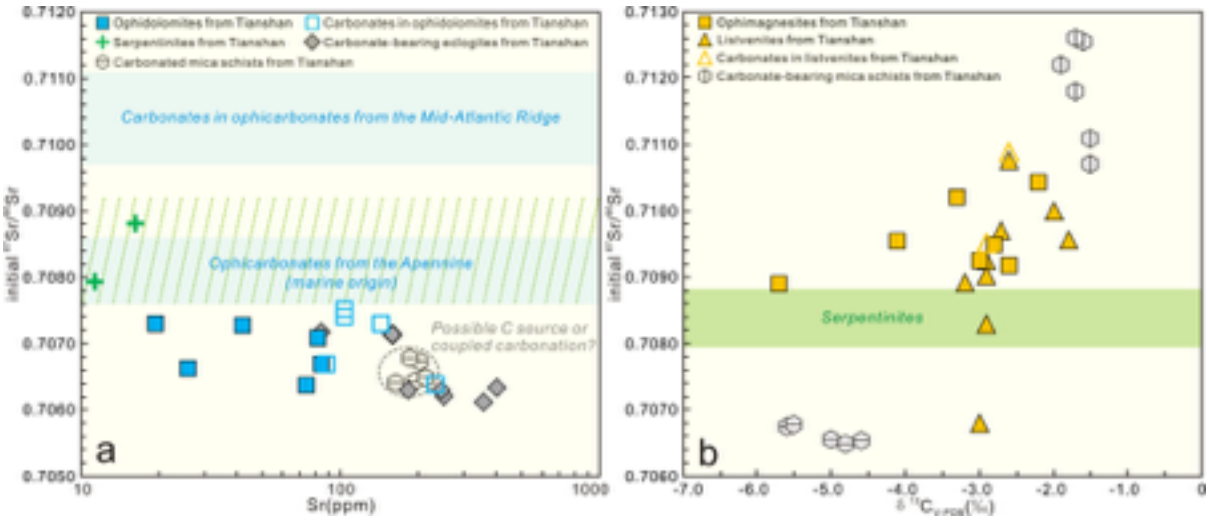
Ophidiolomites from Tianshan
Carbonates in ophidiolomites from Tianshan
Serpentinites from Tianshan
Carbonate-bearing eclogites from Tianshan
Carbonated mica schists from Tianshan
Carbonates in ophicarbonates from the Mid-Atlantic Ridge
Ophicarbonates from the Apennine (marine origin)
Possible C source or coupled carbonation?
a
Sr(ppm)
Ophimagnesites from Tianshan
Listvenites from Tianshan
Carbonates in listvenites from Tianshan
Carbonate-bearing mica schists from Tianshan
Serpentinites
b

**Figure 7**

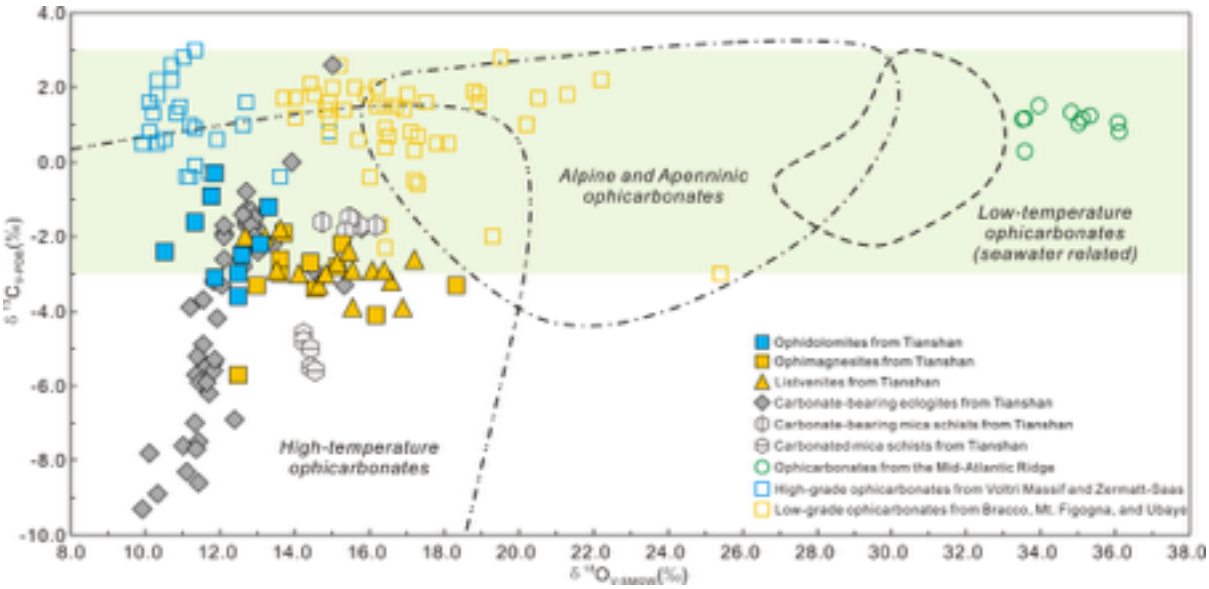
Alpine and Apenninic ophicarbonates
Low-temperature ophicarbonates (seawater related)
High-temperature ophicarbonates
Ophidolomites from Tianshan
Ophimagnesites from Tianshan
Listvenites from Tianshan
Carbonate-bearing eclogites from Tianshan
Carbonate-bearing mica schists from Tianshan
Carbonated mica schists from Tianshan
Ophicarbonates from the Mid-Atlantic Ridge
High-grade ophicarbonates from Voltri Massif and Zermatt-Saas
Low-grade ophicarbonates from Bracco, Mt. Figogna, and Ubaye
4.0
2.0
0.0
-2.0
-4.0
-6.0
-8.0
-10.0
8.0
10.0
12.0
14.0
16.0
18.0
20.0
22.0
24.0
26.0
28.0
30.0
32.0
34.0
36.0
38.0

**Figure 8**

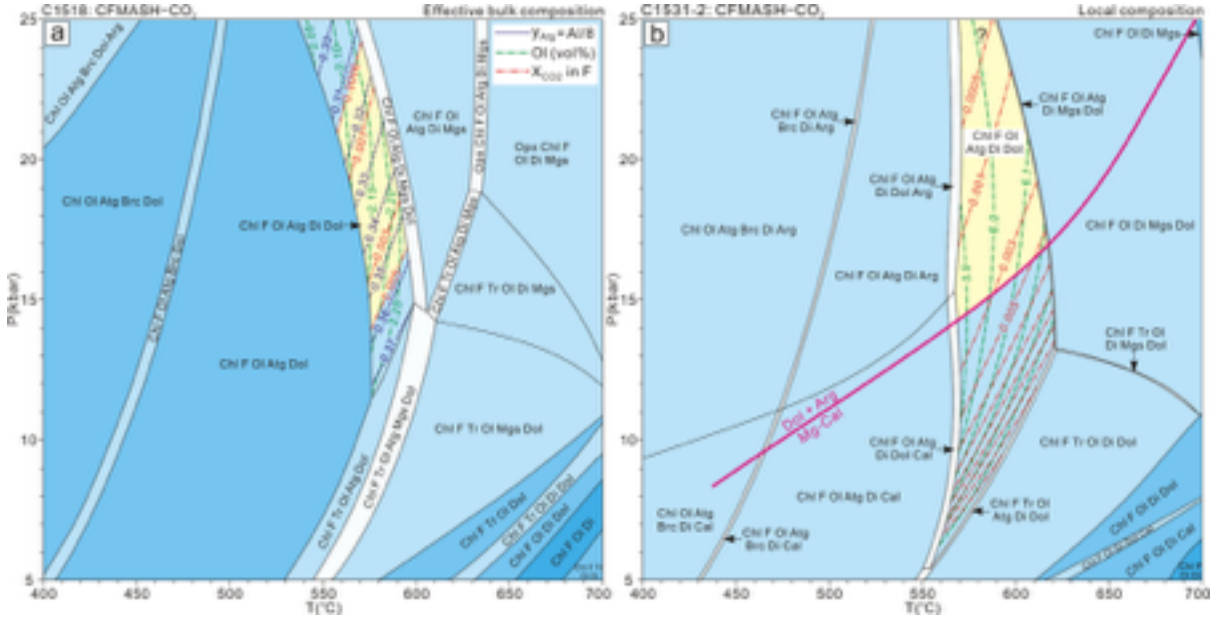
C1518: CFMASH-CO2
Effective bulk composition
a
Chl Ol Atg Brc Dol Arg
Chl Ol Atg Brc Dol
Chl F Ol Atg Di Dol
Chl F Ol Atg Dol
Chl F Ol Atg Di Mgs
Opx Chl F Ol Di Mgs
Chl F Tr Ol Di Mgs
Chl F Tr Ol Mgs Dol
Chl F Tr Ol Di Dol
Chl F Ol Di Dol
Chl F Ol Di
P (kbar)
T(°C)
C1531-2: CFMASH-CO2
Local composition
b
Chl F Ol Di Mgs
Chl F Ol Atg Brc Di Arg
Chl F Ol Atg Di Mgs Dol
Chl F Ol Atg Di Dol
Chl F Ol Atg Di Dol Arg
Chl Ol Atg Brc Di Arg
Chl F Ol Di Mgs Dol
Chl F Ol Atg Di Arg
Chl F Tr Ol Di Mgs Dol
Dol + Arg
Mg Cal
Chl F Ol Atg Di Dol Cal
Chl F Tr Ol Di Dol
Chl F Ol Atg Di Cal
Chl Ol Atg Brc Di Cal
Chl F Ol Atg Brc Di Cal
Chl F Tr Ol Atg Di Dol
Chl F Ol Di Dol
Chl F Ol Di Cal
P (kbar)
T(°C)

**Figure 9**

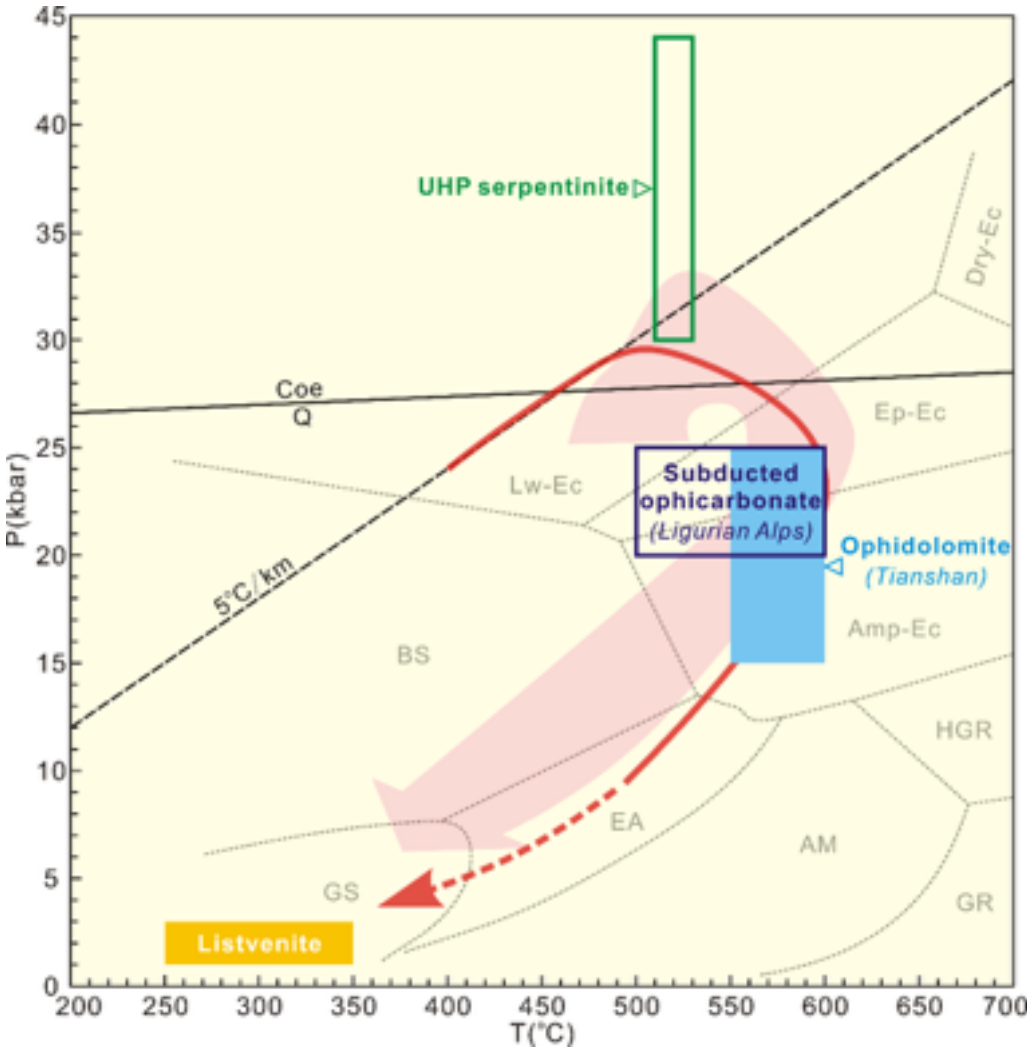
UHP serpentinite
Coe
Q
5°C/km
Subducted
ophicarbonate
(Ligurian Alps)
Ophidolomite
(Tianshan)
Dry-Ec
Ep-Ec
Lw-Ec
Amp-Ec
BS
HGR
EA
AM
GS
GR
Listvenite
P(kbar)
T(°C)
0
5
10
15
20
25
30
35
40
45
200
250
300
350
400
450
500
550
600
650
700

**Figure 10**

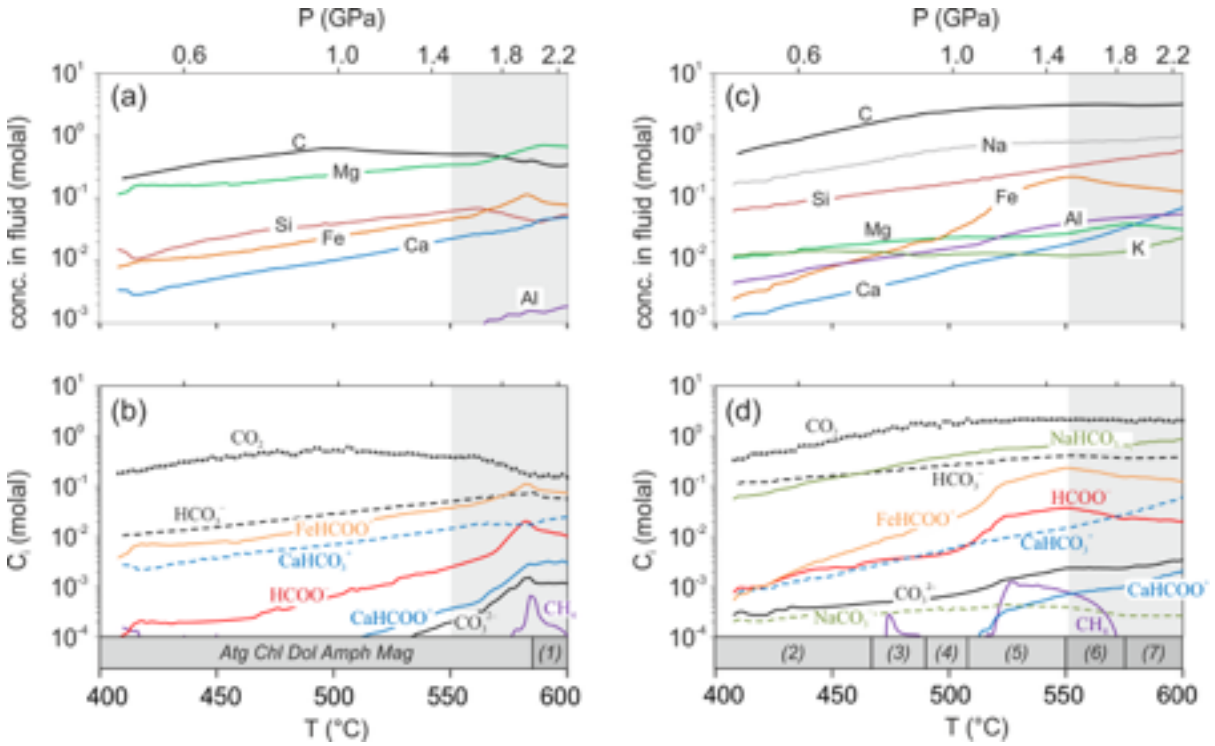
P (GPa)
0.6
1.0
1.4
1.8
2.2
(a)
(b)
(c)
(d)
conc. in fluid (molal)
$C_i$ (molal)
C
Mg
Si
Fe
Ca
Al
Na
K
$CO_2$
$HCO_3^-$
$FeHCOO^+$
$CaHCO_3^+$
HCOO
$CaHCOO^+$
$CO_3^{2-}$
$CH_4$
$NaHCO_3$
$NaCO_3^+$
Atg Chl Dol Amph Mag
(1)
(2)
(3)
(4)
(5)
(6)
(7)
400
450
500
550
600
T (°C)

**Figure 11**

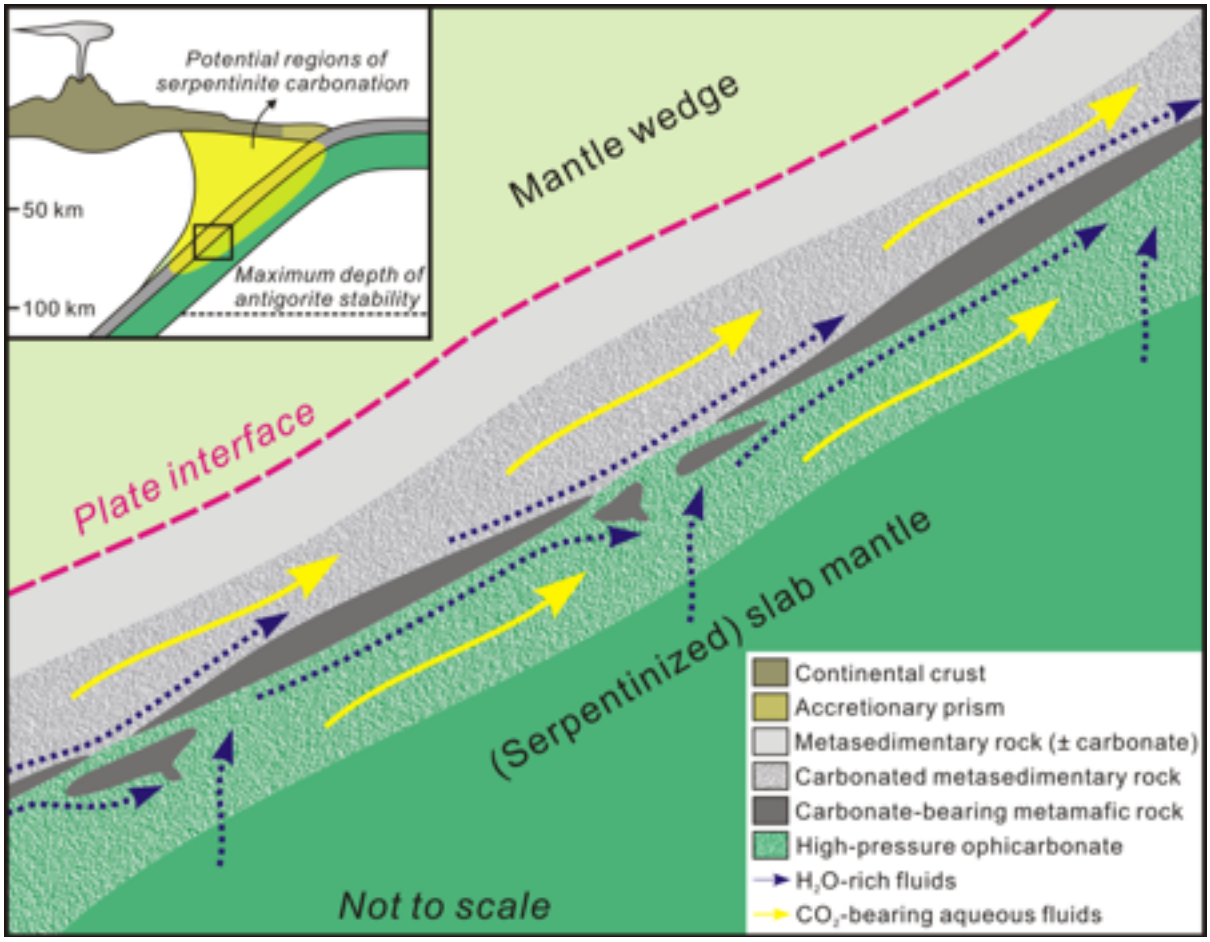
Potential regions of serpentinite carbonation
50 km
100 km
Maximum depth of antigorite stability
Mantle wedge
Plate interface
(Serpentinized) slab mantle
Not to scale
Continental crust
Accretionary prism
Metasedimentary rock (± carbonate)
Carbonated metasedimentary rock
Carbonate-bearing metamafic rock
High-pressure ophicarbonate
H2O-rich fluids
CO2-bearing aqueous fluids

**Figure 12**

**Table 1.** Mineral assemblages and carbonate occurrences of representative carbonated serpentinites from Chinese southwestern Tianshan.

| No. | Sample | Mineral assemblage[a] | Mgs[b] | Dol[b] | Cal[b] | Ol | Atg | Ctl | Di | Chl | Tr | Tlc | Brc | Q | Fuchs | Carbonate occurrence[c] |
|---|---|---|---|---|---|---|---|---|---|---|---|---|---|---|---|---|
| *Ophidolomite* | | | | | | | | | | | | | | | | |
| 1 | C1518 | Atg+Di+Chl+Dol | | C(M) | | | B | | D | A | | | | | | g |
| 2 | C1531-2 | Atg+Di+Chl+Dol+Ca-Dol+Arg+Mg-Cal | | D(T) | E(T) | | C | | B | A | | | | | | g |
| 3 | C1537 | Atg+Chl+Dol+Cal+Brc | | D(m) | B(M) | | A | | | E | | | C | | | g |
| 4 | C1622 | Atg+Di+Chl+Dol+Cal | | E(T) | C(M) | | A | | B | D | | | | | | g+dv |
| 5 | C1641 | Atg+Tr+Dol+Cal | | B(M) | D(T) | | A | | | | C | | | | | g+ccv |
| 6 | C1674-1 | Ol+Atg+Di+Chl+Dol+Cal | | F(T) | E(M) | B | A | | D | C | | | | | | g+dv |
| *Ophimagnesite* | | | | | | | | | | | | | | | | |
| 7 | C1513-2 | Atg+Mgs+Dol+Tlc | B(M) | D(T) | | | A | | | | | C | | | | g |
| 8 | C1515-1 | Atg+Mgs | B(M) | | | | A | | | | | | | | | g |
| 9 | C1612 | Atg+Ctl+Mgs | B(M) | | | | A | C | | | | | | | | g+ccv |
| 10 | C1627-2 | Atg+Mgs | B(M) | | | | A | | | | | | | | | g |
| 11 | C1657 | Atg+Mgs+Tlc | B(M) | | | | A | | | | | C | | | | ccv |
| 12 | C1661-3 | Atg+Mgs | B(M) | | | | A | | | | | | | | | g+dv |
| 13 | C1680 | Atg+Mgs+Dol | B(M) | C(m) | | | A | | | | | | | | | g+dv |
| *Listvenite* | | | | | | | | | | | | | | | | |
| 14 | C1503 | Mgs+Dol+Fuchs+Q | A(M) | B(M) | | | | | | | | | | C | D | g+dv |
| 15 | C1505-2 | Mgs+Dol+Fuchs+Q | A(M) | B(M) | | | | | | | | | | C | D | g+dv |
| 16 | C1517-1 | Mgs+Dol+Fuchs+Q | A(M) | B(M) | | | | | | | | | | C | D | g+dv |
| 17 | C1523 | Mgs+Dol+Fuchs+Q | A(M) | B(M) | | | | | | | | | | C | D | g+dv |

| | | | | | | | | | |
|---|---|---|---|---|---|---|---|---|---|
| 18 | C1532-1 | Mgs+Fuchs+Q | A(M) | | | | B | C | g+dv |
| 19 | C1536 | Mgs+Fuchs+Q | A(M) | | | | B | C | g+dv |

**Table 1 (continued)**

| | | | | | | | | | |
|---|---|---|---|---|---|---|---|---|---|
| 20 | C1541-1 | Mgs+Dol+Fuchs+Q | A(M) | C(M) | | | B | D | g+dv |
| 21 | C1550 | Mgs+Fuchs+Q | A(M) | | | | B | C | g+dv |
| 22 | C1664-1 | Mgs+Fuchs+Chl+Q | A(M) | | | D | B | C | g+dv |

Mineral contents are shown in a decreasing sequence from A to F (A representing the highest content while F representing the lowest content).

Mineral assemblage[a]: Mgs = magnesite, Dol = dolomite, Ca-Dol = Ca-rich dolomite, Arg = aragonite, Mg-Cal = Mg-calcite, Cal = calcite, Ol = olivine, Atg = antigorite, Ctl = chrysotile, Di = diopside, Chl = chlorite, Tr = tremolite, Tlc = talc, Brc = brucite, Q = quartz, Fuchs = fuchsite.

Mgs[b]Dol[b]Cal[b]: M = major carbonate phase (> 5 vol%), m = minor carbonate phase (1–5 vol%), T = trace carbonate phase (< 1 vol%).

Carbonate occurrence[c]: g = grain, dv = discontinuous vein, ccv = cross-cutting vein.

**Table 2.** Representative mineral compositions of carbonated serpentinites from Chinese southwestern Tianshan.

| Rock | Ophidolomite | | | | | | | | | | | | | | | | | |
|---|---|---|---|---|---|---|---|---|---|---|---|---|---|---|---|---|---|---|
| Sampl | C1518 | | | | C1531-2 | | | | | | | | | C1537 | | C1641 | | |
| Minera | Dol | Atg | Chl | Di | Dol | Ca- | Arg | Mg- | Mg- | Mg- | Atg | Chl | Di | Cal | Brc | Dol | Atg | Tr |
| *Mineral compositions (wt%)* | | | | | | | | | | | | | | | | | | |
| $SiO_2$ | 0.0 | 42.0 | 31. | 53.7 | 0.0 | 0.06 | 0.0 | 0.09 | 0.14 | 0.18 | 43.0 | 32. | 55. | 0.0 | 0.0 | 0.0 | 43.1 | 59. |
| $TiO_2$ | 0.0 | 0.02 | 0.0 | 0.79 | 0.0 | 0.04 | 0.0 | 0.04 | 0.02 | 0.03 | 0.02 | 0.0 | 0.0 | 0.0 | 0.0 | 0.0 | 0.00 | 0.0 |
| $Al_2O_3$ | 0.0 | 2.70 | 15. | 0.02 | 0.0 | 0.01 | 0.0 | 0.00 | 0.00 | 0.01 | 2.24 | 14. | 0.0 | 0.0 | 0.0 | 0.0 | 1.61 | 0.0 |
| $Cr_2O_3$ | 0.0 | 0.06 | 0.8 | 0.03 | 0.0 | 0.02 | 0.0 | 0.04 | 0.03 | 0.00 | 0.01 | 0.0 | 0.0 | 0.0 | 0.0 | 0.0 | 0.90 | 0.0 |
| $Fe_2O_3$ | n.d. | n.d. | n.d. | n.d. | n.d. | n.d. | n.d. | n.d. | n.d. | n.d. | n.d. | n.d. | n.d. | n.d. | n.d. | n.d. | n.d. | n.d. |
| FeO | 2.6 | 7.36 | 6.6 | 2.70 | 0.1 | 0.09 | 0.1 | 0.13 | 0.21 | 0.14 | 2.67 | 3.8 | 0.7 | 0.0 | 4.4 | 2.3 | 6.54 | 2.7 |
| MnO | 0.4 | 0.15 | 0.0 | 0.31 | 0.7 | 1.52 | 0.0 | 0.12 | 0.13 | 0.12 | 0.06 | 0.0 | 0.0 | 0.0 | 0.1 | 0.2 | 0.04 | 0.1 |
| MgO | 20. | 34.8 | 31. | 17.2 | 22. | 14.0 | 0.0 | 5.76 | 4.33 | 5.62 | 39.2 | 35. | 17. | 0.1 | 74. | 21. | 35.5 | 22. |
| CaO | 31. | 0.02 | 0.0 | 25.3 | 34. | 41.8 | 56. | 51.76 | 47.42 | 50.34 | 0.01 | 0.0 | 25. | 57. | 0.0 | 33. | 0.03 | 12. |
| $Na_2O$ | 0.0 | 0.03 | 0.0 | 0.00 | 0.0 | 0.01 | 0.0 | 0.01 | 0.02 | 0.00 | 0.00 | 0.0 | 0.0 | 0.0 | 0.0 | 0.0 | 0.01 | 0.5 |
| $K_2O$ | 0.0 | 0.03 | 0.0 | 0.00 | 0.0 | 0.00 | 0.0 | 0.00 | 0.00 | 0.00 | 0.03 | 0.0 | 0.0 | 0.0 | 0.0 | 0.0 | 0.00 | 0.0 |
| Total | 55. | 87.3 | 86. | 100. | 57. | 57.6 | 56. | 57.95 | 52.30 | 56.44 | 87.2 | 86. | 99. | 57. | 79. | 57. | 87.7 | 98. |
| *Cations* | | | | | | | | | | | | | | | | | | |
| Si | 0.0 | 33.0 | 3.0 | 1.96 | 0.0 | 0.00 | 0.0 | 0.003 | 0.005 | 0.006 | 33.0 | 3.1 | 2.0 | 0.0 | 0.0 | 0.0 | 33.5 | 8.0 |
| Ti | 0.0 | 0.01 | 0.0 | 0.02 | 0.0 | 0.00 | 0.0 | 0.001 | 0.001 | 0.001 | 0.01 | 0.0 | 0.0 | 0.0 | 0.0 | 0.0 | 0.00 | 0.0 |
| Al | 0.0 | 2.50 | 1.7 | 0.00 | 0.0 | 0.00 | 0.0 | 0.000 | 0.000 | 0.000 | 2.02 | 1.6 | 0.0 | 0.0 | 0.0 | 0.0 | 1.47 | 0.0 |
| Cr | 0.0 | 0.03 | 0.0 | 0.00 | 0.0 | 0.00 | 0.0 | 0.001 | 0.001 | 0.000 | 0.00 | 0.0 | 0.0 | 0.0 | 0.0 | 0.0 | 0.55 | 0.0 |
| $Fe^{3+}$ | 0.0 | n.c. | 0.0 | 0.03 | 0.0 | 0.00 | 0.0 | 0.000 | 0.000 | 0.000 | n.c. | 0.0 | 0.0 | 0.0 | 0.0 | 0.0 | n.c. | 0.0 |
| $Fe^{2+}$ | 0.0 | 4.84 | 0.4 | 0.04 | 0.0 | 0.00 | 0.0 | 0.003 | 0.006 | 0.004 | 1.71 | 0.2 | 0.0 | 0.0 | 0.0 | 0.0 | 4.26 | 0.3 |
| Mn | 0.0 | 0.10 | 0.0 | 0.01 | 0.0 | 0.03 | 0.0 | 0.003 | 0.004 | 0.003 | 0.03 | 0.0 | 0.0 | 0.0 | 0.0 | 0.0 | 0.02 | 0.0 |
| Mg | 0.9 | 40.9 | 4.5 | 0.93 | 0.9 | 0.62 | 0.0 | 0.266 | 0.223 | 0.267 | 44.9 | 4.9 | 0.9 | 0.0 | 0.9 | 0.9 | 41.2 | 4.5 |
| Ca | 1.0 | 0.01 | 0.0 | 0.98 | 1.0 | 1.33 | 1.9 | 1.722 | 1.759 | 1.719 | 0.00 | 0.0 | 1.0 | 1.9 | 0.0 | 1.0 | 0.02 | 1.8 |
| Na | 0.0 | 0.04 | 0.0 | 0.00 | 0.0 | 0.00 | 0.0 | 0.001 | 0.001 | 0.000 | 0.00 | 0.0 | 0.0 | 0.0 | 0.0 | 0.0 | 0.01 | 0.1 |
| K | 0.0 | 0.03 | 0.0 | 0.00 | 0.0 | 0.00 | 0.0 | 0.000 | 0.000 | 0.000 | 0.02 | 0.0 | 0.0 | 0.0 | 0.0 | 0.0 | 0.00 | 0.0 |
| Sum | 2 | 82 | 10 | 4 | 2 | 2 | 2 | 2 | 2 | 2 | 82 | 10 | 4 | 2 | 1 | 2 | 81 | 15 |
| O | 0 | 116 | 14 | 6 | 0 | 0 | 0 | 0 | 0 | 0 | 116 | 14 | 6 | 0 | 2 | 0 | 116 | 23 |
| $X_{Mg}$ | 0.9 | 0.89 | 0.9 | 0.95 | 1.0 | 1.00 | | | | | 0.96 | 0.9 | 0.9 | | 0.9 | 0.9 | 0.91 | 0.9 |
| $X_{MgCO3}$ | 0.4 | | | | 0.4 | 0.32 | 0.0 | 0.13 | 0.11 | 0.13 | | | | 0.0 | | 0.4 | | |

$X_{Mg}$ = Mg/(Mg + Fe); $X_{MgCO3}$ = Mg/(Ca + Mg + Fe); n.d. = not determined; n.c. = not calculated.

**Table 2 (continued)**

| Rock type | Ophimagnesite | | | | Listvenite | | | |
|---|---|---|---|---|---|---|---|---|
| Sample | C1513-2 | | | | C1541-1 | | | C1664-1 |
| Mineral | Mgs | Mgs | Atg | Tlc | Mgs | Mgs | Dol | Fuchs |
| *Mineral compositions (wt%)* | | | | | | | | |
| $SiO_2$ | 0.02 | 0.01 | 43.07 | 61.37 | 0.00 | 0.05 | 0.00 | 50.56 |
| $TiO_2$ | 0.00 | 0.00 | 0.00 | 0.00 | 0.00 | 0.01 | 0.05 | 0.16 |
| $Al_2O_3$ | 0.00 | 0.00 | 0.55 | 0.04 | 0.03 | 0.01 | 0.00 | 22.38 |
| $Cr_2O_3$ | 0.01 | 0.00 | 0.10 | 0.00 | 0.04 | 0.01 | 0.03 | 10.56 |
| $Fe_2O_3$ | n.d. | n.d. | n.d. | n.d. | n.d. | n.d. | n.d. | n.d. |
| FeO | 4.31 | 11.13 | 7.48 | 2.97 | 2.35 | 9.10 | 4.29 | 0.36 |
| MnO | 0.78 | 0.40 | 0.03 | 0.00 | 0.06 | 0.21 | 0.18 | 0.05 |
| MgO | 46.18 | 42.15 | 35.94 | 29.07 | 47.51 | 43.12 | 20.42 | 3.19 |
| CaO | 0.12 | 0.14 | 0.03 | 0.01 | 0.03 | 0.13 | 30.65 | 0.02 |
| $Na_2O$ | 0.00 | 0.02 | 0.00 | 0.02 | 0.00 | 0.04 | 0.00 | 0.39 |
| $K_2O$ | 0.00 | 0.00 | 0.00 | 0.00 | 0.02 | 0.02 | 0.02 | 8.48 |
| Total | 51.42 | 53.85 | 87.20 | 93.48 | 50.04 | 52.70 | 55.64 | 96.15 |
| *Cations* | | | | | | | | |
| Si | 0.001 | 0.000 | 33.920 | 4.003 | 0.000 | 0.001 | 0.000 | 3.381 |
| Ti | 0.000 | 0.000 | 0.000 | 0.000 | 0.000 | 0.000 | 0.001 | 0.008 |
| Al | 0.000 | 0.000 | 0.510 | 0.003 | 0.001 | 0.000 | 0.000 | 1.765 |
| Cr | 0.000 | 0.000 | 0.062 | 0.000 | 0.001 | 0.000 | 0.001 | 0.558 |
| $Fe^{3+}$ | 0.000 | 0.000 | n.c. | 0.000 | 0.000 | 0.000 | 0.000 | 0.014 |
| $Fe^{2+}$ | 0.098 | 0.256 | 4.926 | 0.162 | 0.054 | 0.210 | 0.107 | 0.006 |
| Mn | 0.018 | 0.009 | 0.020 | 0.000 | 0.001 | 0.005 | 0.005 | 0.003 |
| Mg | 1.879 | 1.729 | 42.197 | 2.826 | 1.941 | 1.776 | 0.907 | 0.318 |
| Ca | 0.004 | 0.004 | 0.025 | 0.001 | 0.001 | 0.004 | 0.979 | 0.001 |
| Na | 0.000 | 0.001 | 0.000 | 0.003 | 0.000 | 0.002 | 0.000 | 0.051 |
| K | 0.000 | 0.000 | 0.000 | 0.000 | 0.001 | 0.001 | 0.001 | 0.724 |
| Sum | 2 | 2 | 82 | 7 | 2 | 2 | 2 | 7 |
| O | 0 | 0 | 116 | 11 | 0 | 0 | 0 | 11 |
| $X_{Mg}$ | 0.95 | 0.87 | 0.90 | 0.95 | 0.97 | 0.89 | 0.89 | 0.98 |
| $X_{MgCO3}$ | 0.95 | 0.87 | | | 0.97 | 0.89 | 0.46 | |

$X_{Mg}$ = Mg/(Mg + Fe); $X_{MgCO3}$ = Mg/(Ca + Mg + Fe); n.d. = not determined; n.c. = not calculated.

**Table 3.** Sr isotope compositions of serpentinites and carbonated serpentinites from Chinese southwestern Tianshan.

| Sample | Rock type | Measurement | Rb (ppm) | Sr (ppm) | $(^{87}Sr/^{86}Sr)_m$[a] | 2σ | $^{87}Rb/^{86}Sr$ | $(^{87}Sr/^{86}Sr)_{320Ma}$ | $(^{87}Sr/^{86}Sr)_{290Ma}$ |
|---|---|---|---|---|---|---|---|---|---|
| C1509-b | Serpentinite | Whole rock | 0.10 | 11.30 | 0.708049 | 0.000020 | 0.025 | 0.707935 | 0.707946 |
| C1619-2 | Serpentinite | Whole rock | 0.09 | 16.20 | 0.708885 | 0.000016 | 0.016 | 0.708814 | 0.708820 |
| C1518 | Ophidolomite | Whole rock | 0.07 | 19.35 | 0.707348 | 0.000007 | 0.010 | 0.707301 | — |
| C1518 | Ophidolomite | Carbonate | 0.28 | 144.00 | 0.707323 | 0.000006 | 0.006 | 0.707298 | — |
| C1531-2 | Ophidolomite | Whole rock | 0.14 | 25.79 | 0.706694 | 0.000007 | 0.015 | 0.706624 | — |
| C1537 | Ophidolomite | Whole rock | 0.06 | 82.13 | 0.707096 | 0.000012 | 0.002 | 0.707087 | — |
| C1537 | Ophidolomite | Carbonate | 0.05 | 104.00 | 0.707529 | 0.000007 | 0.001 | 0.707523 | — |
| C1622 | Ophidolomite | Whole rock | 0.22 | 42.12 | 0.707343 | 0.000034 | 0.015 | 0.707276 | — |
| C1622 | Ophidolomite | Carbonate | 1.22 | 104.00 | 0.707555 | 0.000008 | 0.033 | 0.707404 | — |
| C1641 | Ophidolomite | Whole rock | 0.11 | 84.66 | 0.706708 | 0.000039 | 0.004 | 0.706691 | — |
| C1641 | Ophidolomite | Carbonate | 0.16 | 88.40 | 0.706719 | 0.000007 | 0.005 | 0.706696 | — |
| C1674-1 | Ophidolomite | Whole rock | 0.003 | 73.78 | 0.706377 | 0.000027 | 0.0001 | 0.706376 | — |
| C1674-1 | Ophidolomite | Carbonate | 0.05 | 234.00 | 0.706388 | 0.000007 | 0.001 | 0.706385 | — |
| C1513-2 | Ophimagnesite | Whole rock | 0.04 | 71.79 | 0.709503 | 0.000016 | 0.002 | — | 0.709497 |
| C1515-1 | Ophimagnesite | Whole rock | 0.03 | 118.40 | 0.709549 | 0.000019 | 0.001 | — | 0.709546 |
| C1612 | Ophimagnesite | Whole rock | 0.07 | 256.62 | 0.710426 | 0.000010 | 0.001 | — | 0.710423 |
| C1627-2 | Ophimagnesite | Whole rock | 0.12 | 74.30 | 0.708917 | 0.000057 | 0.005 | — | 0.708898 |
| C1657 | Ophimagnesite | Whole rock | 0.10 | 40.59 | 0.710226 | 0.000013 | 0.007 | — | 0.710197 |
| C1661-3 | Ophimagnesite | Whole rock | 0.13 | 22.70 | 0.709305 | 0.000057 | 0.016 | — | 0.709238 |
| C1680 | Ophimagnesite | Whole rock | 0.49 | 85.92 | 0.709238 | 0.000119 | 0.016 | — | 0.709172 |
| C1503 | Listvenite | Whole rock | 8.27 | 477.40 | 0.710187 | 0.000009 | 0.049 | — | 0.709985 |

**Table 3 (continued)**

| | | | | | | | | | |
|---|---|---|---|---|---|---|---|---|---|
| C1505-2 | Listvenite | Whole rock | 2.25 | 378.13 | 0.709634 | 0.000008 | 0.017 | — | 0.709565 |
| C1517-1 | Listvenite | Whole rock | 18.28 | 721.64 | 0.710000 | 0.000010 | 0.072 | — | 0.709705 |
| C1523 | Listvenite | Whole rock | 10.35 | 340.21 | 0.709609 | 0.000134 | 0.086 | — | 0.709254 |
| C1523 | Listvenite | Carbonate | 1.24 | 284.80 | 0.709552 | 0.000022 | 0.012 | — | 0.709501 |
| C1532-1 | Listvenite | Whole rock | 0.46 | 97.55 | 0.708976 | 0.000019 | 0.013 | — | 0.708921 |
| C1536 | Listvenite | Whole rock | 5.93 | 123.92 | 0.711318 | 0.000022 | 0.135 | — | 0.710761 |
| C1536 | Listvenite | Carbonate | 0.76 | 102.01 | 0.710964 | 0.000020 | 0.021 | — | 0.710877 |
| C1541-1 | Listvenite | Whole rock | 6.09 | 877.66 | 0.709099 | 0.000011 | 0.020 | — | 0.709018 |
| C1550 | Listvenite | Whole rock | 1.89 | 126.09 | 0.708473 | 0.000013 | 0.042 | — | 0.708298 |
| C1664-1 | Listvenite | Whole rock | 0.70 | 23.80 | 0.707134 | 0.000014 | 0.083 | — | 0.706791 |

$(^{87}Sr/^{86}Sr)_m$[a] = measured $^{87}Sr/^{86}Sr$ ratios.

**Table 4.** C and O isotope compositions of carbonates in carbonated serpentinites from Chinese southwestern Tianshan.

| Sample | Rock type | $\delta^{13}C_{V\text{-}PDB}$ (‰) | $\delta^{18}O_{V\text{-}SMOW}$ (‰) |
|---|---|---|---|
| C1518 | Ophidolomite | -3.6 | 12.5 |
| C1537 | Ophidolomite | -2.5 | 12.6 |
| C1621 | Ophidolomite | -2.2 | 13.1 |
| C1622 | Ophidolomite | -0.3 | 11.8 |
| C1634-4 | Ophidolomite | -3.1 | 11.8 |
| C1641 | Ophidolomite | -2.4 | 10.5 |
| C1654 | Ophidolomite | -3.0 | 12.5 |
| C1674-1 | Ophidolomite | -1.6 | 11.3 |
| C1674-2 | Ophidolomite | -1.2 | 13.3 |
| C16-7.27-1 | Ophidolomite | -0.9 | 11.7 |
| C1507-1 | Ophimagnesite | -3.4 | 14.5 |
| C1513-2 | Ophimagnesite | -2.8 | 15.1 |
| C1515-1 | Ophimagnesite | -4.1 | 16.2 |
| C1612 | Ophimagnesite | -2.2 | 15.2 |
| C1627-2 | Ophimagnesite | -5.7 | 12.5 |
| C1636-2 | Ophimagnesite | -1.9 | 13.7 |
| C1657 | Ophimagnesite | -3.3 | 18.3 |
| C1661-3 | Ophimagnesite | -3.0 | 13.6 |
| C1680 | Ophimagnesite | -2.6 | 13.6 |
| C16-8.2-1 | Ophimagnesite | -3.3 | 13.0 |
| C16-8.2-2 | Ophimagnesite | -2.7 | 14.4 |

**Table 4 (continued)**

| | | | |
|---|---|---|---|
| C1503 | Listvenite | -2.0 | 13.2 |
| C1505-2 | Listvenite | -1.8 | 13.6 |
| C1517-1 | Listvenite | -2.7 | 15.1 |
| C1523 | Listvenite | -2.9 | 16.1 |
| C1532-1 | Listvenite | -3.2 | 16.6 |
| C1536 | Listvenite | -2.6 | 17.2 |
| C1540 | Listvenite | -3.0 | 14.1 |
| C1541-1 | Listvenite | -2.9 | 13.5 |
| C1550 | Listvenite | -2.9 | 15.5 |
| C1655 | Listvenite | -3.9 | 16.9 |

| | | | |
|---|---|---|---|
| C1656-2 | Listvenite | -2.9 | 16.4 |
| C1662 | Listvenite | -3.3 | 14.6 |
| C1664-1 | Listvenite | -3.0 | 14.8 |
| C1672 | Listvenite | -2.0 | 12.7 |
| C1677 | Listvenite | -3.9 | 15.5 |
| C1682 | Listvenite | -2.4 | 15.4 |

**Table 5.** Bulk and local compositions of representative carbonated serpentinites from Chinese southwestern Tianshan.

| Sample | $SiO_2$ | $TiO_2$ | $Al_2O_3$ | $TFe_2O_3$[a] | MnO | MgO | CaO | $Na_2O$ | $K_2O$ | $P_2O_5$ | LOI | Total |
|---|---|---|---|---|---|---|---|---|---|---|---|---|
| *ICP-OES analyses (wt%)* | | | | | | | | | | | | |
| HP ophidolomite C1518 | 32.24 | 0.09 | 11.87 | 7.37 | 0.10 | 32.25 | 1.77 | 0.25 | 0.01 | 0.04 | 14.01 | 100.00 |
| HP ophidolomite C1531-2 | 36.77 | 0.58 | 9.81 | 6.17 | 0.16 | 33.03 | 2.90 | 0.30 | 0.05 | 0.13 | 10.23 | 100.13 |
| LP ophimagnesite C1661-3 | 37.16 | 0.02 | 0.98 | 8.33 | 0.07 | 37.01 | 0.05 | 0.01 | 0.01 | 0.02 | 15.39 | 99.05 |
| LP listvenite C1541-1 | 35.08 | 0.07 | 2.51 | 5.25 | 0.08 | 20.86 | 6.41 | 0.12 | 0.42 | 0.03 | 29.25 | 100.08 |

| Sample | $SiO_2$ | $TiO_2$ | $Al_2O_3$ | FeO | $Fe_2O_3$ | MnO | MgO | CaO | $Na_2O$ | $K_2O$ | $P_2O_5$ | $H_2O$ | $CO_2$ | Total |
|---|---|---|---|---|---|---|---|---|---|---|---|---|---|---|
| *Effective bulk-rock compositions derived from mineral compositions and modes (wt%)* | | | | | | | | | | | | | | |
| HP ophidolomite C1518 | 32.83 | – | 12.08 | 6.70 | – | – | 32.42 | 1.65 | – | – | – | 11.79 | 2.53 | 100.00 |
| LP listvenite C1541-1 | 35.32 | – | 2.76 | 3.35 | – | – | 21.06 | 6.64 | – | 0.33 | – | 0.22 | 30.32 | 100.00 |
| *Local composition derived from mineral compositions and modes (wt%)* | | | | | | | | | | | | | | |
| HP ophidolomite C1531-2 | 40.17 | – | 8.37 | 2.76 | – | – | 28.45 | 10.63 | – | – | – | 7.84 | 1.78 | 100.00 |

$TFe_2O_3$[a] = total Fe.

# Supplementary materials to:

## Multistage $CO_2$ sequestration in the subduction zone: insights from exhumed carbonated serpentinites, SW Tianshan UHP belt, China

Weigang Peng [a,b], Lifei Zhang [a*], Manuel D. Menzel [c],

Alberto Vitale Brovarone [d], Simone Tumiati [b], Tingting Shen [e], Han Hu [a]

[a] *MOE Key Laboratory of Orogenic Belts and Crustal Evolution, School of Earth and Space Sciences, Peking University, Beijing 100871, China*

[b] *Dipartimento di Scienze della Terra, Università degli Studi di Milano, via Mangiagalli 34, 20133, Milano, Italy*

[c] *Instituto Andaluz de Ciencias de la Tierra (IACT), CSIC-UGR, Av. Palmeras 4, 18100 Armilla, Spain*

[d] *Institut de Minéralogie, de Physique des Matériaux et de Cosmochimie UMR 7590 CNRS-UPMC-IRD-MNHN, Campus Jussieu, Case courrier 115, 4 Place Jussieu, 75005 Paris, France*

[e] *Institute of Geology, Chinese Academy of Geological Sciences, Beijing 100037, China*

[*]**Corresponding author**

Lifei Zhang; E-mail:lfzhang@pku.edu.cn

**Supplementary figure captions**

Supplementary Fig. S1. $T–X_{CO2}$ pseudosections calculated in the CFMASH–$CO_2$ system (with saturated $H_2O$ and $CO_2$) at 2 GPa for homogeneous ophidolomite C1518 using (a) measured and (b) effective bulk compositions. Mineral assemblages in the numbered fields: (1) Chl Ol Atg Dol, (2) Chl Ol Atg Mgs Dol, (3) Chl Atg Di Mgs Dol, (4) Opx Chl Atg Di Mgs, (5) Opx Chl Tr Atg Mgs, (6) Opx Chl Ol Di Mgs, (7) Opx Chl Tr Di Mgs, and (8) Chl Mgs Law Q.

Supplementary Fig. S2. Phase diagrams calculated in the CFMASH–$CO_2$ system for HP ophidolomites from the study area. (a) *P–T* pseudosection for homogeneous ophidolomite C1518 based on the integrated Ol-existing bulk composition. Isopleths of the Al content of antigorite ($y_{Atg}$ = Al/8 in a.p.f.u., blue dotted line; Padrón-Navarta et al., 2013) and $X_{CO2}$ in fluids (red stippled line) are contoured in the pseudosection. (b) *P–T* pseudosection for inhomogeneous ophidolomite C1531-2 based on the integrated Ol-existing local composition. The aragonite–Mg-calcite transition (pink solid line) was experimentally determined by Hermann et al. (2016).

Supplementary Fig. S3. Temperature estimates of the retrograde reequilibration Dol + Arg → Mg-Cal based on the composition of Mg-calcite in the ophidolomite C1531 (modified from Hermann et al., 2016). The X(Mg) isopleths of Mg-calcite coexistent with aragonite (green dotted line) or dolomite (blue dotted line) are shown. Stars A and B represent $X_{MgCO3}$ values of Mg-calcite in this study. The compiled *P–T* paths (grey arrow lines) and estimated peak *P–T* conditions (grey boxes) of the Chinese southwestern Tianshan are from Tan et al. (2017).

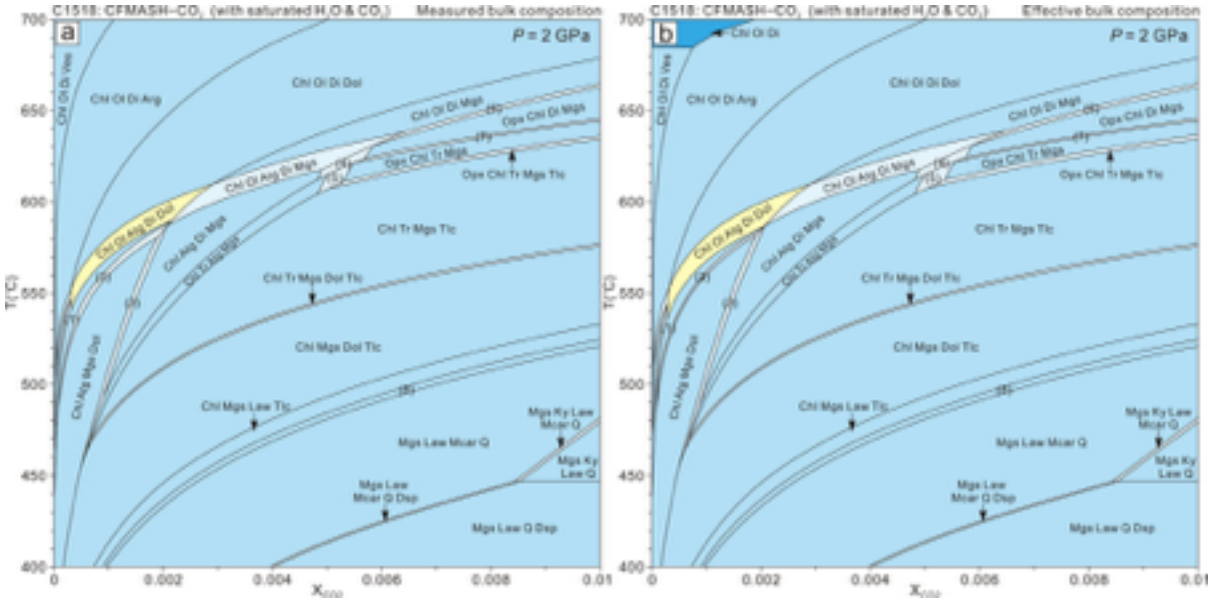


**Supplementary figure S1**

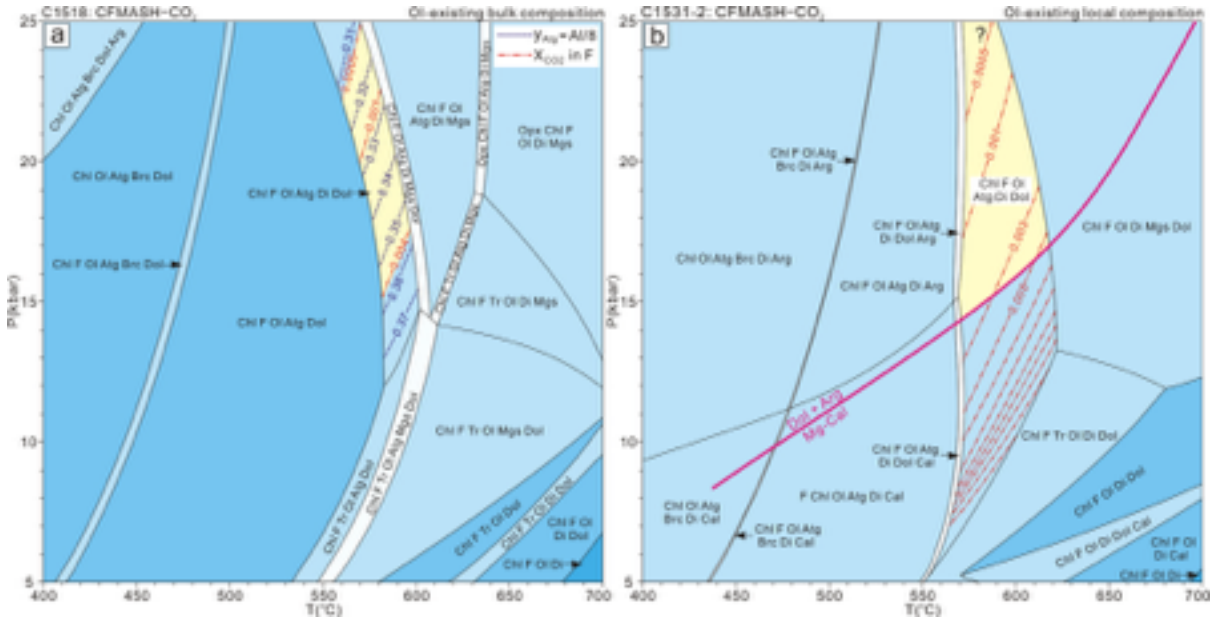


**Supplementary figure S2**

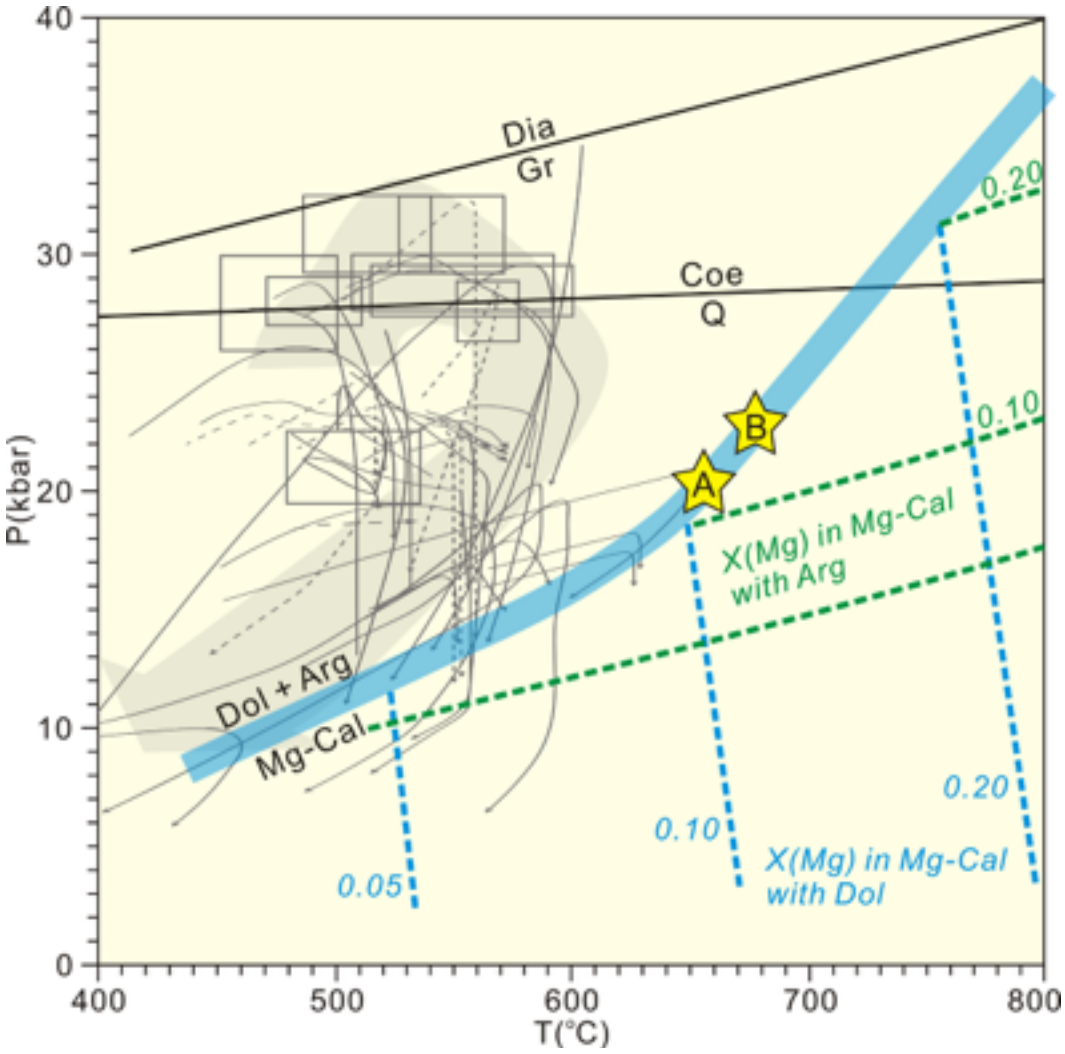


**Supplementary figure S3**

**Supplementary Table S1.** Solution models used for thermodynamic modelling.

| Phase | Perple_X | Used for[a] | Type/Comment | Source |
|---|---|---|---|---|
| olivine | Ol(HP) | A, B, C | | Holland and Powell (1998) |
| orthopyrox | Opx(HP) | A, B, C | speciation model | Holland and Powell (1996) |
| clinopyrox | Cpx(HP) | A, B, C | disordered | Holland and Powell (1996) |
| omphacite | Omph(GHP) | D | | Green et al. (2007) |
| garnet | Gt(WPH) | D | | White et al. (2007) |
| chlorite | Chl(HP) | A, B, C, D | speciation model | Holland et al. (1998) |
| antigorite | Atg(PN) | A, B, C | ideal, tschermak | Padrón-Navarta et al. (2013) |
| carbonate | oCcM(EF) | A, B, C, D | ternary speciation model | Franzolin et al. (2011) |
| amphibole | Amph(DHP) | A, B, C | | Dale et al. (2000) |
| amphibole | Amph(DPW) | D | | Dale et al. (2005) |
| epidote | Ep(HP) | D | | Holland and Powell (1998) |
| mica | Mica(CHA) | D | | Coggon and Holland (2002) |
| feldspar | feldspar | D | | Fuhrman and Lindsley |
| talc | T | B, C | ideal | |
| brucite | B | A, B, C | ideal | |
| magnetite | MF | C, D | ideal | |
| binary | F | A | $H_2O$–$CO_2$ | Holland and Powell (1991) |
| COH-fluid | COH-Fluid+ | C, D | $H_2O$–$CO_2$–$CH_4$ with non-linear subdivision and aqueous speciation | Connolly and Galvez (2018) |

Aragonite, diaspore, kyanite, lawsonite, magnesiocarpholite, quartz, and vesuvianite were taken to be pure phases.

Used for[a]: solution models used for the calculation of (A) $P$–$T$ conditions of ophidolomite; (B) $T$–$X_{CO_2}$

**Supplementary Table S2.** Integrated olivine-existing bulk (C1518) and local (C1531-2) compositions of HP ophidolomites from Chinese southwestern Tianshan.

| Sample | $SiO_2$ | $TiO_2$ | $Al_2O_3$ | FeO | $Fe_2O_3$ | MnO | MgO | CaO | $Na_2O$ | $K_2O$ | $P_2O_5$ | $H_2O$ | $CO_2$ | Total |
|---|---|---|---|---|---|---|---|---|---|---|---|---|---|---|
| HP ophidolomite C1518 | 32.86 | – | 11.96 | 6.72 | – | – | 32.80 | 1.64 | – | – | – | 11.50 | 2.52 | 100.00 |
| HP ophidolomite C1531-2 | 40.06 | – | 8.17 | 3.11 | – | – | 29.37 | 10.47 | – | – | – | 7.06 | 1.76 | 100.00 |

## References


Coggon R. and Holland T. J. B. (2002) Mixing properties of phengitic micas and revised garnet-phengite thermobarometers. *J. Metamorph. Geol.* **20**, 683–696.

Connolly J. A. D. and Galvez M. E. (2018) Electrolytic fluid speciation by Gibbs energy minimization and implications for subduction zone mass transfer. *Earth Planet. Sci. Lett.* **501**, 90–102.

Dale J., Holland T. J. B. and Powell R. (2000) Hornblende–garnet–plagioclase thermobarometry: a natural assemblage calibration of the thermodynamics of hornblende. *Contrib. Mineral. Petrol.* **140**, 353–362.

Dale J., Powell R., White R. W., Elmer F. L. and Holland T. J. B. (2005) A thermodynamic model for Ca–Na clinoamphiboles in $Na_2O$–CaO–FeO–MgO–$Al_2O_3$–$SiO_2$–$H_2O$–O for petrological calculations. *J. Metamorph. Geol.* **23**, 771–791.

Franzolin E., Schmidt M. W. and Poli S. (2011) Ternary Ca–Mg–Fe carbonates: subsolidus phase relations at 3.5 GPa and a thermodynamic solid solution model including order/disorder. *Contrib. Mineral. Petrol.* **161**, 213–227.

Fuhrman M. L. and Lindsley D. H. (1988) Ternary-feldspar modeling and thermometry. *Am. Mineral.* **73**, 201–215.

Green E., Holland T. and Powell R. (2007) An order–disorder model for omphacitic pyroxenes in the system jadeite–diopside–hedenbergite–acmite, with applications to eclogitic rocks. *Am. Mineral.* **92**, 1181–1189.

Hermann J., Troitzsch U. and Scott D. (2016) Experimental subsolidus phase relations in the system $CaCO_3$–$CaMg(CO_3)_2$ up to 6.5 GPa and implications for subducted marbles. *Contrib. Mineral. Petrol.* **171**. https://doi.org/10.1007/s00410-016-1296-y.

Holland T. and Powell R. (1991) A Compensated-Redlich-Kwong (CORK) equation for volumes and fugacities of $CO_2$ and $H_2O$ in the range 1 bar to 50 kbar and 100–1600°C. *Contrib. Mineral. Petrol.* **109**, 265–273.

Holland T. and Powell R. (1996) Thermodynamics of order–disorder in minerals: II. Symmetric formalism applied to solid solutions. *Am. Mineral.* **81**, 1425–1437.

Holland T. J. B. and Powell R. (1998) An internally consistent thermodynamic data set for phases of petrological interest. *J. Metamorph. Geol.* **16**, 309–343.

Holland T., Baker J. and Powell R. (1998) Mixing properties and activity–composition relationships of chlorites in the system MgO–FeO–$Al_2O_3$–$SiO_2$–$H_2O$. *Eur. J. Mineral.* **10**, 395–406.

Li J. L., Klemd R., Gao J. and Meyer M. (2014) Compositional zoning in dolomite from lawsonite-bearing eclogite (SW Tianshan, China): Evidence for prograde metamorphism during subduction of oceanic crust. *Am. Mineral.* **99**, 206–217.

Padrón-Navarta J. A., López Sánchez-Vizcaíno V., Hermann J., Connolly J. A. D., Garrido C. J., Gómez-Pugnaire, M. T. and Marchesi C. (2013) Tschermak's substitution in antigorite and consequences for phase relations and water liberation in high-grade serpentinites. *Lithos* **178**, 186–196.

Tan Z., Agard P., Gao J., John T., Li J., Jiang T., Bayet L., Wang X. and Zhang X. (2017) P–T–time-isotopic evolution of coesite-bearing eclogites: Implications for exhumation processes in SW Tianshan. *Lithos* **278–281**, 1–25.

White R. W., Powell R. and Holland T. J. B. (2007) Progress relating to calculation of partial melting equilibria for metapelites. *J. Metamorph. Geol.* **25**, 511–527.